NASA/TM—2019-220340

LCF Life of As-Deposited and Annealed NiCr-Y Coatings for Oxidation and Hot Corrosion Protection of Disk Alloys

James A. Nesbitt, Timothy P. Gabb, and Susan L. Draper
Glenn Research Center, Cleveland, Ohio

Robert A. Miller
Vantage Partners, LLC, Brook Park, Ohio

Ivan E. Locci
University of Toledo, Toledo, Ohio

Chantal K. Sudbrack
Glenn Research Center, Cleveland, Ohio

November 2019

NASA STI Program . . . in Profile

Since its founding, NASA has been dedicated to the advancement of aeronautics and space science. The NASA Scientific and Technical Information (STI) Program plays a key part in helping NASA maintain this important role.

The NASA STI Program operates under the auspices of the Agency Chief Information Officer. It collects, organizes, provides for archiving, and disseminates NASA's STI. The NASA STI Program provides access to the NASA Technical Report Server—Registered (NTRS Reg) and NASA Technical Report Server—Public (NTRS) thus providing one of the largest collections of aeronautical and space science STI in the world. Results are published in both non-NASA channels and by NASA in the NASA STI Report Series, which includes the following report types:

- TECHNICAL PUBLICATION. Reports of completed research or a major significant phase of research that present the results of NASA programs and include extensive data or theoretical analysis. Includes compilations of significant scientific and technical data and information deemed to be of continuing reference value. NASA counter-part of peer-reviewed formal professional papers, but has less stringent limitations on manuscript length and extent of graphic presentations.

- TECHNICAL MEMORANDUM. Scientific and technical findings that are preliminary or of specialized interest, e.g., "quick-release" reports, working papers, and bibliographies that contain minimal annotation. Does not contain extensive analysis.

- CONTRACTOR REPORT. Scientific and technical findings by NASA-sponsored contractors and grantees.

- CONFERENCE PUBLICATION. Collected papers from scientific and technical conferences, symposia, seminars, or other meetings sponsored or co-sponsored by NASA.

- SPECIAL PUBLICATION. Scientific, technical, or historical information from NASA programs, projects, and missions, often concerned with subjects having substantial public interest.

- TECHNICAL TRANSLATION. English-language translations of foreign scientific and technical material pertinent to NASA's mission.

For more information about the NASA STI program, see the following:

- Access the NASA STI program home page at http://www.sti.nasa.gov

- E-mail your question to help@sti.nasa.gov

- Fax your question to the NASA STI Information Desk at 757-864-6500

- Telephone the NASA STI Information Desk at 757-864-9658

- Write to:
  NASA STI Program
  Mail Stop 148
  NASA Langley Research Center
  Hampton, VA 23681-2199

NASA/TM—2019-220340

LCF Life of As-Deposited and Annealed NiCr-Y Coatings for Oxidation and Hot Corrosion Protection of Disk Alloys

James A. Nesbitt, Timothy P. Gabb, and Susan L. Draper
Glenn Research Center, Cleveland, Ohio

Robert A. Miller
Vantage Partners, LLC, Brook Park, Ohio

Ivan E. Locci
University of Toledo, Toledo, Ohio

Chantal K. Sudbrack
Glenn Research Center, Cleveland, Ohio

National Aeronautics and
Space Administration

Glenn Research Center
Cleveland, Ohio 44135

November 2019

This work was sponsored by the Advanced Air Vehicle Program
at the NASA Glenn Research Center

Level of Review: This material has been technically reviewed by technical management.

Available from

NASA STI Program
Mail Stop 148
NASA Langley Research Center
Hampton, VA 23681-2199

National Technical Information Service
5285 Port Royal Road
Springfield, VA 22161
703-605-6000

This report is available in electronic form at http://www.sti.nasa.gov/ and http://ntrs.nasa.gov/

LCF Life of As-Deposited and Annealed NiCr-Y Coatings for Oxidation and Hot Corrosion Protection of Disk Alloys

James A. Nesbitt*, Timothy P. Gabb, and Susan L. Draper*
National Aeronautics and Space Administration
Glenn Research Center
Cleveland, Ohio 44135

Robert A. Miller
Vantage Partners, LLC
Brook Park, Ohio 44142

Ivan E. Locci
University of Toledo
Toledo, Ohio 43606

Chantal K. Sudbrack†
National Aeronautics and Space Administration
Glenn Research Center
Cleveland, Ohio 44135

Abstract

Increasing temperatures in aero gas turbines is resulting in oxidation and hot corrosion attack of turbine disks. Since disks are sensitive to low cycle fatigue (LCF), any environmental attack, and especially hot corrosion pitting, can seriously degrade the life of the disk. Application of metallic coatings is one means of protecting disk alloys from this environmental attack. However, the presence of a metallic coating can degrade the LCF life of a disk alloy. Therefore, coatings must be designed which are not only resistant to oxidation and corrosion attack, but do not significantly degrade the LCF life of the alloy.

Three different NiCr-Y coating compositions (29, 35.5, 44 wt% Cr, all with 0.1 wt% Y) were applied at two thicknesses by Plasma Enhanced Magnetron Sputtering (PEMS) to two similar Ni-based disk alloys. One Ni-35.5Cr-0.1Y coating also received a thin ZrO_2 overcoat. The coated samples were also given a short thermal anneal in a low partial pressure of oxygen to encourage bonding of the coating and substrate as well as initiating formation of a chromia scale. Without further environmental exposure, the LCF life of coated and uncoated samples was evaluated at 760 °C in air. The LCF lifetime of all coated samples was less than that of uncoated samples. The LCF life scaled with the Cr content and the high-Cr, thin coating showed the highest LCF life. Pre and post-test characterization of the various coatings, including identification of crack initiation sites, will be presented and the effect of the coating on the LCF life discussed.

*Retired
†Formerly with NASA Glenn Research Center

Introduction

Temperatures in aero gas-turbine engines continue to rise in order to improve fuel efficiency and reduce NOx emissions (Refs. 1 to 5). Although these higher temperatures can have operational and efficiency benefits, the elevated temperatures can also result in increased environmental attack. In the turbine section of current engines, peak blade temperatures can reach 1050 to 1200 °C (Refs. 5 and 6). Because of the high temperatures, turbine blades and vanes are typically protected by metallic coatings for protection from oxidation and hot corrosion. Metallic coatings for blades, either aluminides or MCrAlY (M = Ni,Co) overlays, typically form alumina (Al_2O_3) surface scales which provide excellent oxidation protection at the elevated temperatures associated with the blades (Ref. 5). Hot corrosion of blades or vanes in modern aero engines is often not a problem because the high temperatures prevent salt from condensing on the blades, and cleaner fuels have significantly reduced S levels. Where corrosion might be an issue, such as for airlines servicing airports near oceans or seas resulting in the ingesting of sea salt, the Cr in MCrAlY coatings or modifications to an aluminide coating (e.g., Pt-aluminides) help to provide corrosion protection (Refs. 7 and 8).

Although turbine disks operate at significantly lower temperatures than blades and vanes, the push for higher efficiencies and cleaner exhausts has resulted in disk temperatures in advanced commercial aero engines reaching temperatures of 704 °C (Refs. 9 and 10) with goals for achieving temperatures of 760 °C (Refs. 2, 9, 11, and 12). At these higher temperatures, disk alloys will experience oxidation attack, and in certain environments, hot corrosion as well (Refs. 1, 4, 13 to 15). Unlike turbine blades and vanes, turbine disks have historically remained uncoated due to their lower operating temperatures, however options to provide environmental protection for higher temperatures without use of coatings are limited. One obvious possibility is to increase the amount of environmentally beneficial elements, such as Cr, Al, and Ta to the alloy. However, for both blade and disk materials, the alloys have already been compositionally optimized to increase the mechanical strength by maximizing the volume fraction of the ordered γ' phase while also increasing the amount of refractory elements (e.g., Ti, Ta, W, and Nb) to strengthen both the γ and γ' phases (Refs. 6 and 16). Unfortunately, this increase in mechanical strength has come at the expense of the environmentally-beneficial Cr level (Refs. 5, 6, and 16).

The alternative to alloying is typically to apply coatings, which, as stated above, have been successfully used for many decades with blades and vanes (Refs. 5, 17, and 18). But, applying the same coatings developed for blades onto disks could degrade critical properties of disks. Blades, operating at higher temperatures than disks, are more susceptible to creep. To counteract this mechanical mode of degradation, blades in advanced engines are cast and directionally solidified or solidified as single crystals (Ref. 6). However, disks are limited by low cycle fatigue (LCF) (Refs. 9, 19, and 20). Hence, advanced disks are fabricated by powder metallurgy techniques to improve microstructural uniformity and provide a fine grain microstructure for both high strength and fatigue resistance (Refs. 12 and 21). Grain boundaries are furthered strengthened against cracking by formation of carbides (primarily $M_{23}C_6$). Since fatigue damage starts with crack initiation, disks are susceptible to any type of defect that could initiate a crack. Therefore, great effort has been expended to minimize any internal oxide inclusions or surface defects, which might initiate a crack (Refs. 22 to 24). Furthermore, shot peening of the surface is routinely used to induce a compressive stress in the near-surface region of the disk to inhibit both crack initiation and crack propagation (Ref. 25). Alumina-forming aluminide or MCrAlY coatings, designed for higher temperature protection of blades, could be too brittle or have too high of a surface roughness, which could initiate fatigue cracks.

Hence, a coating optimized for disks is required to provide environmental protection. Since disks have not been routinely coated, previous relevant work on the effect of environmental exposures and the effect of coatings on the fatigue life of various Ni-base superalloys will be briefly reviewed. This review will then be followed by specific requirements for a disk coating and conclude with the purpose of this study.

Effect of Oxidation and Hot Corrosion on Fatigue Life

Oxidation has been clearly shown to reduce the low cycle fatigue life (LCF) of Ni-based superalloys (Refs. 3, 9, 26 to 37). Not surprisingly, surface initiated cracking typically increases with increasing oxidation attack (Refs. 31 and 32), where cracking eventually initiates in thicker, brittle oxide scales and propagates into the substrate (Refs. 26, 29, and 35). In addition, the selective oxidation of the oxygen-active elements, such as Al and Ti, at the surface result in the formation of a near-surface γ layer depleted of the strengthening γ' phase. This weaker γ phase can be susceptible to enhanced crack initiation and growth (Refs. 14, 26, 29, 35, and 38). Once cracks initiate at the surface, oxidation and corrosion within the crack and at the crack tip produce brittle crack propagation paths accelerating the crack growth (Refs. 39 to 42). When the cracks propagate in an intergranular fashion, this oxidation along the grain boundaries can remove grain boundary carbides and produce fine voids as well as fine, recrystallized grains (Refs. 4, 31, 39, and 40). The end result of the oxidation exposure is that both crack initiation and crack propagation is accelerated.

Hot corrosion of Ni-base alloys can occur in the presence of certain salts (e.g., Na_2SO_4, NaCl) and sulfur (S). This hot corrosion is typically separated by mechanism and morphology into two temperature regimes: Type I occurring at higher temperatures generally in the range of 800 to 950 °C, and Type II occurring in the temperature range of disk operation of 650 to 800 °C (Refs. 1, 18, 43 to 45). Because of the higher temperatures, Type I attack in aero engines has usually been associated with blades and vanes whereas Type II attack has been observed in cooler regions of the blade, such as below platforms. Because of the higher gas temperatures being experienced in aero engines, Type II hot corrosion attack is beginning to be observed in the higher-temperature regions of disks (i.e., the rim). The trademark of this lower temperature Type II attack is a layer of non-protective Ni and Co oxide above a layer or pit filled with metal sulfides, but without the internal sulfide particles such as are present with Type I attack (Refs. 4, 5, and 46). Although the traditional trademark for Type II corrosion is pit formation, other studies have shown that the corrosion morphology can vary from isolated pitting to a more uniform surface attack based on the environment (e.g., SO_2/SO_3 concentration) (Ref. 47) or exposure time (Ref. 48). Other studies have shown that for a given set of conditions, sulfides can be present below the sulfate layers and with the addition of stress, V-shaped notches can be formed rather than the traditional rounded pit (Ref. 46).

Hot corrosion has long been known to reduce the LCF life of Ni base alloys (Refs. 1, 13, 46, 49 to 58). Specifically, Type II hot corrosion resulting in pits was shown to shorten fatigue life due to crack initiation at the bottom of pits (Refs. 15, 55, and 59). Although current aviation fuels have reduced S levels below that in past decades, air quality over certain industrialized cities has worsened resulting in the intake of S-containing gasses into the aircraft engines servicing those cities (Ref. 20). As a result, hot corrosion has been reported on the higher temperature, outer rim area of disks in certain engines. Once cracks initiate, continued corrosion, or oxidation in the crack can accelerate crack propagation. The effect of hot corrosion on reducing the fatigue life has been shown to be affected by many variables including the temperature, salt chemistry and salt loading, SO_2 pressure, and stress/strain range (Refs. 46 and 49). Although the operating temperatures of disks (e.g., 650 to 700 °C) is relatively low in comparison to that of blades, it is apparent that both oxidation and hot corrosion can significantly degrade the LCF life of disk alloys.

Effect of Coatings on Fatigue Life

Many coatings have been investigated for providing environmental protection for various Ni-base superalloys undergoing fatigue. Without any environmental exposure, the effect of the coating on the fatigue life has varied from detrimental to beneficial, sometimes changing behavior for the same coating with temperature, stress, or strain range (Refs. 38, 60 to 66). It is commonly observed that significantly higher amounts of cracking occur with coated specimens than with uncoated specimens (Refs. 26, 60, and 67). Some of these coating cracks propagate into the substrate resulting in earlier failure before that for uncoated specimens (Refs. 10, 64, and 65). Some of this cracking can be attributed to a lack of ductility in the coating. However, increased cracking is also observed in the more ductile MCrAlY coatings as well. In these cases, the increased cracking has been attributed to a mismatch in material properties (Ref. 26). In certain studies, although increased cracking was present, the benefit of the coating was only observed at low stresses; at higher stresses there was no difference between coated and uncoated samples (Ref. 68).

Other causes of premature failure due to the coating, primarily with aluminide coatings, is reported due to crack initiation at defects such as undesirable phases (Ref. 62) and Kirkendall-type porosity formed in the coating (Ref. 69). Other researchers have reported premature failure due to crack initiation at small grit particles remaining at the interface between the coating and substrate after a standard pre-coat grit blast treatment (Refs. 66 and 70). Although this latter cause of failure is not directly caused by the coating, it should be noted that even a routine and accepted pre-coat treatment such as grit blasting, commonly used before overlay coating deposition by plasma spraying, can have a detrimental effect on the fatigue life.

Coating Requirements for Disks

Since coatings appear to be the most promising means of protecting disks from oxidation and hot corrosion attack, these coatings must be carefully chosen so as to provide adequate environmental protection while minimizing any detrimental effect on the fatigue life (Refs. 5 and 17). Obviously, the overall coating requirement is that the coating must provide oxidation and hot corrosion protection (Ref. 7). This implies formation of either an alumina or chromia scale on the surface. However, coating/substrate interdiffusion, especially for thin coatings, can reduce the level of the Al or Cr in the coating as it diffuses into the substrate, while undesirable elements (e.g., Mo or Ti) from the substrate can diffuse to the coating surface degrading the oxidation and corrosion protection. Therefore, a desirable, but challenging requirement for a coating would be low interdiffusion rates between the coating and substrate, or the inclusion of a diffusion barrier (Ref. 5).

The second general requirement of a coating is that it must have a minimal detrimental effect on the LCF life of the disk (Refs. 19 and 61). This requirement has several aspects. First, surface cracking in the coating must be minimized since oxidation and hot corrosion attack can occur within the cracks resulting in more rapid crack propagation leading to failure. Therefore, since brittle coatings are more likely to crack, coatings with a high ductile-brittle transition temperature (DBTT) are to be avoided. Similarly, cracking can result from a mismatch in the materials properties between the coating and substrate. Hence, material properties (e.g., Young's modulus, yield strength, coefficient of thermal) between the coating and substrate should be matched as best as possible.

Another requirement is that coating formation (e.g., for aluminides), or post-coat interdiffusion of the coating and disk, should not produce any deleterious phases, such as topologically close-packed (TCP) or acicular-shaped (Ref. 62) phases which could initiate or help propagate cracks in the coating. Likewise, any coating deposition process or pre-coat treatment, which results in cracks, pores, or foreign debris within the coating or at the coating/substrate interface, should also be avoided or the defects minimized.

These internal defects, which can initiate cracks, have been observed as Kirkendall porosity associated with aluminide formation (Ref. 69), oxide particles within the coating associated with plasma spraying, and oxide grit remaining at the coating/substrate interface following a pre-coat grit blast of the surface (Refs. 66 and 70). Another requirement concerns the roughness of the surface after coating. It is well known that oxidation and hot corrosion will typically result in surface initiated cracking since the environmental attack can change the surface morphology (e.g., pitting or grain boundary oxidation) (Ref. 14). The number of potential crack initiation sites at the surface is enhanced with a rough surface. Therefore, the coating surface should be as smooth as possible before any environmental exposures in order to minimize surface initiated cracking (Ref. 13). This requirement also applies to the surface roughness following a post-coat processing treatment, such as shot peening, so that any benefit of the treatment be balanced with any potential increase in surface cracking due to increased surface roughness (Ref. 13). Furthermore, coating/substrate interdiffusion (C/S) should not result in the recrystallization of the disk, which can result in less-than-optimal grain sizes or loss of important grain boundary strengthening carbides reducing the resistance of the substrate to crack initiation and propagation. Lastly, temperatures during coating formation or post-coat anneals must not significantly affect the disk microstructure (i.e., grain size, grain boundary carbides, etc.) which has been optimized for strength and fatigue resistance. For instance, some aluminide processing, or MCrAlY post-coat diffusion anneals are carried out at temperatures at or above 1000 °C which could coarsen the size of the fine γ' particles of the disk alloy.

Hence, some obvious coating requirements for protecting disks are:

(1) Coatings must provide oxidation and hot corrosion protection at the temperatures of interest with low rates of C/S interdiffusion.
(2) Coatings must not significantly degrade the LCF behavior of the disk substrate.
    a. Ductile coating with a low DBTT
    b. Good coefficient of thermal and material property match to the disk substrate
    c. Minimal pore or deleterious phase formation
    d. Surface must be as smooth as possible to minimize surface initiated cracking
    e. No substrate recrystallization
    f. Coating deposition or post-coat processing must not significantly affect the disk microstructure.

Since it is generally recognized that aluminide coatings are more brittle (higher DBTT) than MCrAlY coatings (Ref. 17), the latter may be preferred for disks where fatigue is critical. For MCrAlY coatings, CoCrAlY coatings are generally better than NiCrAlY or NiCoCrAlY for providing Type II hot corrosion protection at lower temperatures (Ref. 17). However, CoCrAlY coatings tend to be more brittle than NiCrAlY coatings and possess higher DBTT (Ref. 17) suggesting Ni-based MCrAlY coatings may be preferable for disk applications. The composition of a NiCrAlY-type coating can be adjusted to give a balance between the corrosion resistance and the coating ductility (Ref. 5). In addition, since disk operating temperatures are generally below 750 °C, coatings with significant Cr may be better candidates for hot corrosion protection since Cr is known to provide the best protection against low-temperature, Type II hot corrosion (Refs. 5, 7, 8, 17, 18, 71, and 72). At these intermediate temperatures, higher Cr with lower Al levels should also provide sufficient oxidation protection while increasing ductility. Addition of small amounts of oxygen-active elements (e.g., Y) enhance oxide-scale adhesion and can reduce the oxide growth rate (Refs. 5, 7, and 18).

Consequently, in the present study, NiCr-Y coatings were selected for oxidation and hot corrosion protection of disk alloys. These coatings were selected following the design philosophy stated by Misra (Ref. 11) that a disk coating should be "thin and ductile". Presumably, a NiCr-Y coating would be one of the most ductile of the MCrAlY's while forming a protective Cr_2O_3 scale for both oxidation and hot corrosion protection in the temperature range of interest (700 to 760 °C). It was hoped that the low operational temperatures associated with disks (650 to 750 °C) would minimize interdiffusion since most diffusion barriers consist of thin refractory, oxide, or nitride layers (Ref. 5) which could be brittle, crack and initiate cracks into the substrate. As suggested above, small additions of Y were included primarily to improve oxide scale adhesion (Ref. 7). Interdiffusion of a NiCr-Y coating and typical Ni-base disk superalloys was not expected to precipitate any deleterious phases. Lastly, deposition by physical vapor deposition (PVD) would allow relatively low processing temperatures which would not degrade the microstructure of the disk alloy as well as produce a relatively clean coating free of oxide particles.

Three basic NiCr-Y coating compositions and two different coating thicknesses were examined to determine the effect of both coating composition (Cr content) and coating thickness on the LCF life. Varying the Cr content allowed not only the environmental resistance to be evaluated at three different Cr levels, but also the coating ductility assuming the lower Cr level would be more ductile. Varying the coating thickness would confirm the premise that thin coatings were preferred over thick coatings when evaluating the LCF life. The thinner coating thickness selected in this study (~20 μm) was generally less than that for most MCrAlY overlay coatings (>75 μm). There was also some indication, based on early studies with ZrO_2-Y_2O_3 thermal barrier coatings used in marine engines, that these coatings helped protect against hot corrosion even though the outer portion of the coating spalled leaving only a thin ZrO_2-Y_2O_3 layer. Hence, a thin, outer ZrO_2 layer over the NiCr-Y coating was also examined.

This study is being reported in two parts. This first report describes the coating microstructure and morphology and measured LCF lifetimes with and without the NiCr-Y coatings. Post-test characterization determined the role of the coating in the primary crack initiation site. A following report describes the LCF life after shot peening, oxidation and hot corrosion exposures. Comparison of the LCF lifetimes in both reports was used to identify the most promising coatings for protecting disk alloys.

Experimental

Alloy Composition and Geometry

Two compositionally similar disk alloys, designated LSHR (Ref. 73) and ME3 (Refs. 32 and 74), were used in this study. Typical analyzed compositions are given in Table 1. LCF specimens of these alloys were machined from heat-treated rectangular specimens taken from forged disks. Details of the disk consolidation, heat treatment, and LCF specimen fabrication are given elsewhere (Refs. 15, 16, 73, and 74). Two sizes of the LCF specimens were used; a larger specimen with the ME3 alloy with a test section diameter of 6.35 mm and a smaller, threaded specimen for the LSHR alloy with a test section diameter of 4.80 mm. In addition, 1-2 characterization pins of the ME3 alloy were also coated with each set of LCF specimens. The diameter of the pins was the same as the larger LCF specimen (ϕ = 6.35 mm). Macrographs of the two LCF specimen sizes and a characterization pin are shown in Figure 1. Machining in the reduced diameter test section of the LCF specimens was performed by low stress grinding (LSG) to a surface finish of 0.8 μm Ra (~32 μin. RMS) leaving circumferential grinding marks on the surface which can be detrimental during LCF testing. Hence, the final machining step for both LCF specimen sizes was mechanical polishing in the longitudinal direction to a specified surface finish less than 0.2 μm Ra (~8 μin. RMS) such that all polishing marks were in the longitudinal direction as can be seen in Figure 1(b).

TABLE 1.—COMPOSITION OF LSHR AND ME3 ALLOYS (wt%)

	Ni	Co	Cr	Al	W	Ta	Mo	Nb	Ti	Zr	B	C	S	O_2
LSHR	50.14	20.4	12.3	3.49	4.24	1.59	2.72	1.51	3.48	0.05	0.027	0.047	0.0011	188 ppm
ME3	50.48	20.6	13.0	3.23	1.97	2.38	3.73	0.89	3.59	0.048	0.02	0.057	Not analyzed	Not analyzed

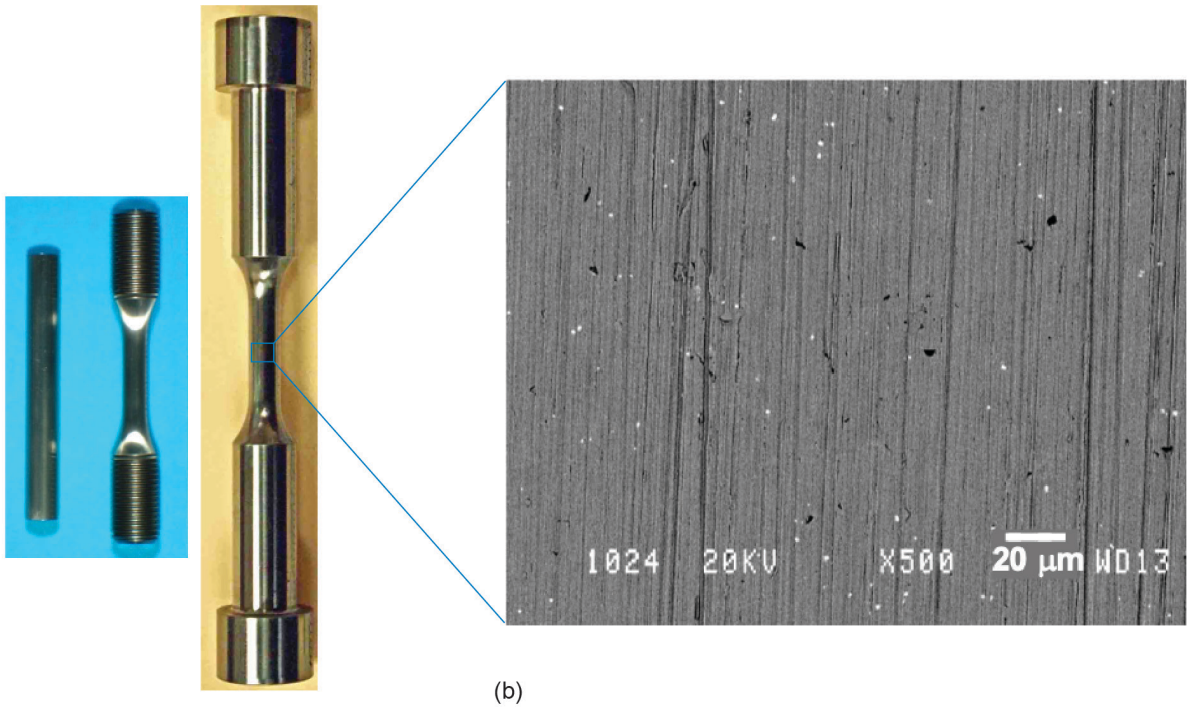

(a) (b)

Figure 1.—(a) Pin, small and large LCF specimens, (b) SEM image of the reduced gage section of an LCF specimen showing the longitudinal polishing marks on a finished LCF specimen.

Typical surface roughness measured on a specimen after the longitudinal polishing was 0.147±0.011 µm Ra[1]. Measurement of the depth of the most prominent scratches on the surface showed depths as great as 1 to 1.3 µm, however, because of the longitudinal orientation of the fine polishing marks, they have not been observed to be a factor in crack initiation of uncoated specimens.

LCF specimens and pins were coated by plasma enhanced magnetron sputtering (PEMS) at the Southwest Research Institute (SwRI) in San Antonio, Texas. The PEMS coater contained two opposing targets in a horizontal orientation so that the samples could be hung and rotated between the targets. For sample fixturing, the coater contained a planetary fixture with six positions, which allowed up to six specimens to be uniformly coated during a single coating run. However, by coupling some of the smaller LCF specimens and pins, up to six specimens (two large, four small) and two pins (coupled to two small specimens) were coated in a single run.

Table 2 shows the coating designations, targets used, resulting coating thicknesses, measured Cr content and the order for the six coating runs. A target of Ni-27Cr-0.1Y was used for five of the runs. For three of these five runs, a pure Cr source was used as a second target. By varying the power to the pure Cr source, higher Cr concentrations in the coatings were produced. For the sixth run, a Ni-35Cr-0.1Y target was used in one target and a Zr source was used as the second target to produce a thin, outer layer of ZrO_2 over the NiCr-Y layer by reactive sputtering with oxygen. Although it is possible that the as-grown

[1]Roughness (Ra) measured using a Zygo NewView 7200 optical profilometer using a 20X objective, Res. 1.10 µm, no filters.

TABLE 2.—COATING DESIGNATIONS, TARGETS, COATING THICKNESSES, CR CONTENT OF DEPOSITED COATINGS AND RUN ORDER

Coating designation	Target 1, wt%	Target 2, wt%	Coating thickness,[a] μm	Cr content of deposited coating,[b] wt%	Run order
Low Cr, ***Thin***	Ni-27.3Cr-0.12Y[c]	----------	20.4±0.6	29.1	1
Med Cr, ***Thin***	Ni-27.3Cr-0.12Y	100% Cr	21.5±0.9	37.0	2
High Cr, ***Thin***	Ni-27.3Cr-0.12Y	100% Cr	19.8±1.9	44.4	3
Low Cr, ***Thick***	Ni-27.3Cr-0.12Y	----------	37.6±4.2	28.9	4
Med Cr, ***Thick***	Ni-27.3Cr-0.12Y	100% Cr	41.0±0.8	35.2	5
Med Cr+ZrO$_2$, ***Thin***	Ni-35Cr-0.15Y[d]	100% Zr[e]	19.3±1.0	34.8	6

[a]Thickness measured on pins after 16N-200 percent shot peen and 8 hr low PO_2 diffusion anneal
[b]Composition measured by EDS
[c]Analyzed composition, nominal given as Ni-28Cr-0.15Y
[d]Nominal composition
[e]Oxygen was bled into the chamber to reactively sputter a thin ZrO_2 layer

Zr-O layer was oxygen deficient after sputtering, it is expected to form stoichiometric ZrO_2 after the short anneal at 760 °C described below and will be referred to as ZrO_2 hereafter. Longer sputter times, as well as higher power to the guns, produced thicker coatings. Hereafter, coatings will primarily be referred to by the coating designation shown in the leftmost column of the table. The ***Low Cr***, ***Thin*** coating will be considered the baseline for both Cr content (29.1 wt%) and thickness (20.4±0.6 μm).

Ends of the LCF specimens were masked with two layers of metal foil so no coating would be deposited on any threaded area or where the grips for LCF testing would be attached (Figure 2). Metallographic cross-sections of the coated pins were used for characterization of the coating composition using a scanning electron microscope (SEM) with energy dispersive spectroscopy (EDS). Coating thicknesses were measured using both optical microscopy and SEM.

Low PO_2 Diffusion Anneal

Each of the coated specimens and pins were given a short thermal anneal at 760 °C for 8 hr in an environment with a low partial pressure of oxygen (PO_2). The purpose for this anneal was two-fold, firstly, to allow some interdiffusion and bonding between the coating and substrate prior to further processing, and secondly, to promote the formation of a Cr_2O_3 oxide scale on the coating surface. The low PO_2 environment was achieved by flowing ultra-high purity (99.999 percent) Ar gas (UHP Ar) past a coil of Ni foil at 760 °C. This procedure was performed in a horizontal tube furnace capable of being evacuated to a pressure <30 mTorr, with repeated backfilling with the UHP Ar. The Ni foil established an equilibrium partial pressure of O_2 equal to that of the free energy of formation of NiO at 760 °C, given as 1.4×10^{-15} atm (Ref. 75) (SGPS - SGTE pure substances database). At this oxygen pressure, only the Cr and Y would oxidize on the surface of the coating. Furnace ramp for heating to 760 °C was 4 hr. The Ni foil was "rejuvenated" approximately every eighth run when annealed samples began showing some tarnish on the surface which usually appeared on the upstream end of an LCF specimen. The Ni foil was rejuvenated by passing Ar-5%H_2 over the coiled Ni at 1000 °C for 6 hr.

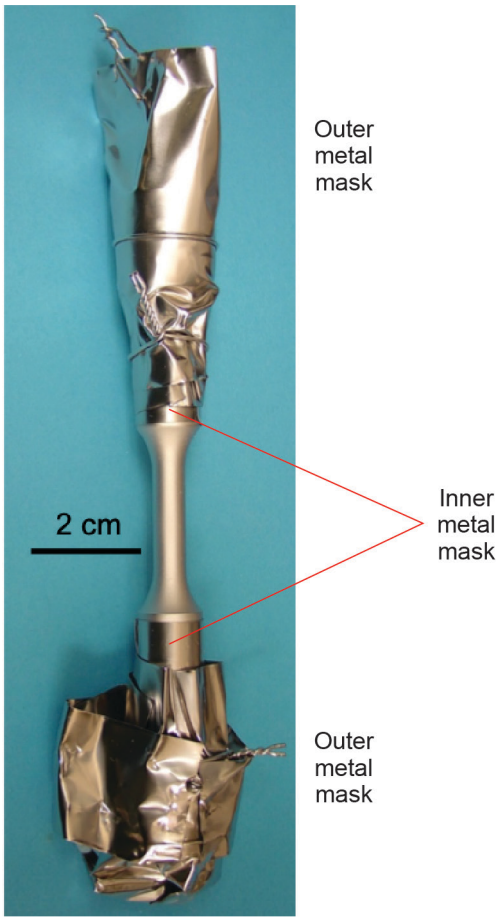

Figure 2.—Large fatigue specimen showing the inner and outer metal masks with exposed test section to be coated.

LCF Testing

Fatigue cycling was conducted in air on all test specimens using a servo-hydraulic test machine with a resistance heated furnace integrated to enclose the specimen and specimen grips. Stress was consistently cycled between maximum and minimum stress values of 841 and –427 MPa in each cycle using a saw-tooth waveform at a frequency of 0.33 Hz. These stresses corresponded to the stabilized maximum and minimum stresses produced by tests run on this material with strain cycled at a strain range of 0.76 percent and strain ratio (minimum/maximum strain) of 0 at 760 °C. However, in the present tests, stress was cycled, and an extensometer was not used to contact the coated specimen surface for measuring strain so as to avoid any contact and interaction with the coating. Previous testing of the ME3 alloy at this strain range at 760 °C resulted primarily in surface-initiated cracks leading to failure (Ref. 32). Hence, this strain range was selected in order to magnify the effect of the coating with regard to surface-initiated cracking leading to failure. Two specimens of each of the six coating compositions were tested. For comparison to a baseline, uncoated specimens were also tested with the longitudinal surface polish. The uncoated specimens did not receive the 8 hr low PO_2 diffusion anneal. After testing, the fracture surfaces were examined using the SEM to examine the location of the primary crack leading to failure. The fractured specimen was then rotated in the SEM and the surface of the LCF specimen was examined in the same area as the primary crack initiation point. This location was selected such that as the primary crack propagated into the specimen, stress in the coating along the axis in either direction from the crack

was relieved and likely showed minimal further growth whereas the cracks opposite the initiation site of the primary crack usually showed wide crack displacements which likely occurred shortly before fracture.

Following the SEM examination of the fracture surface and the side of the specimen, cuts were made in the specimen to allow metallurgical mounting and polishing and the coating. Specimens were examined both perpendicular to the specimen axis as well as parallel to the specimen axis using optical microscopy and SEM, in order to sufficiently evaluate the coating morphology and cracks which had developed in the coating and substrate.

Results

Coating Surface

SEM images of the as-deposited surface of each coating are shown in Figure 3. Small oval defects, commonly referred to as spits (a.k.a. droplets, nodules or macros) (Ref. 76) are evident on each of the coatings with the largest number on the High-Cr, Thin coating. These spits are believed to occur when molten droplets of the target material are ejected due to arcing within the sputtering gun. They are often poorly bonded and lost from the coating becoming a source of a common “pinhole” defect (Ref. 76). It is also apparent in Figure 3 that some of the coatings show fine black lines along the LCF specimen axis. Higher magnification images in Figure 4 show that, in addition to the spits, there is a distinct coating texture following the rod axis with the presence of what appear to be occasional fine cracks along the axis. Since these fine “cracks” form during coating deposition, they will be referred to as linear gaps to differentiate them from fatigue cracks which form perpendicular to the specimen axis during fatigue testing. It appears that the fine texture in the coating, apart from the linear gaps, is reflecting the longitudinal polishing marks originally on the surface of the LCF specimen. This reflection of the substrate surface by the coating was further confirmed by examining the surface of some of the characterization pins, which did not receive a final longitudinal polish but had fine polishing marks

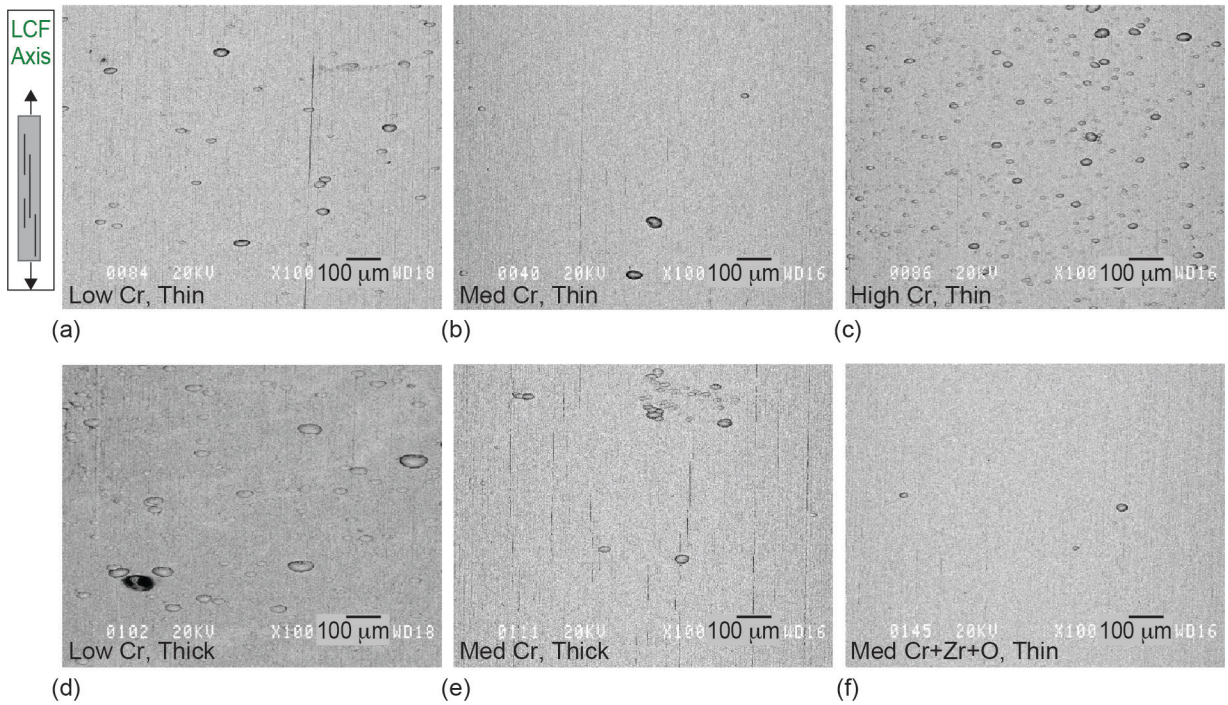

Figure 3.—Low magnification BSE-SEM images of the coated surface for each of the coatings. (a) ***Low Cr, Thin***, (b) ***Med Cr***, ***Thin***, (c) ***High Cr***, ***Thin***, (d) ***Low Cr***, ***Thick***, (e) ***Med Cr***, ***Thick***, (f) ***Med Cr+Zr-O***, ***Thin***. The LCF loading axis is vertical for each of the images as indicated in the inset.

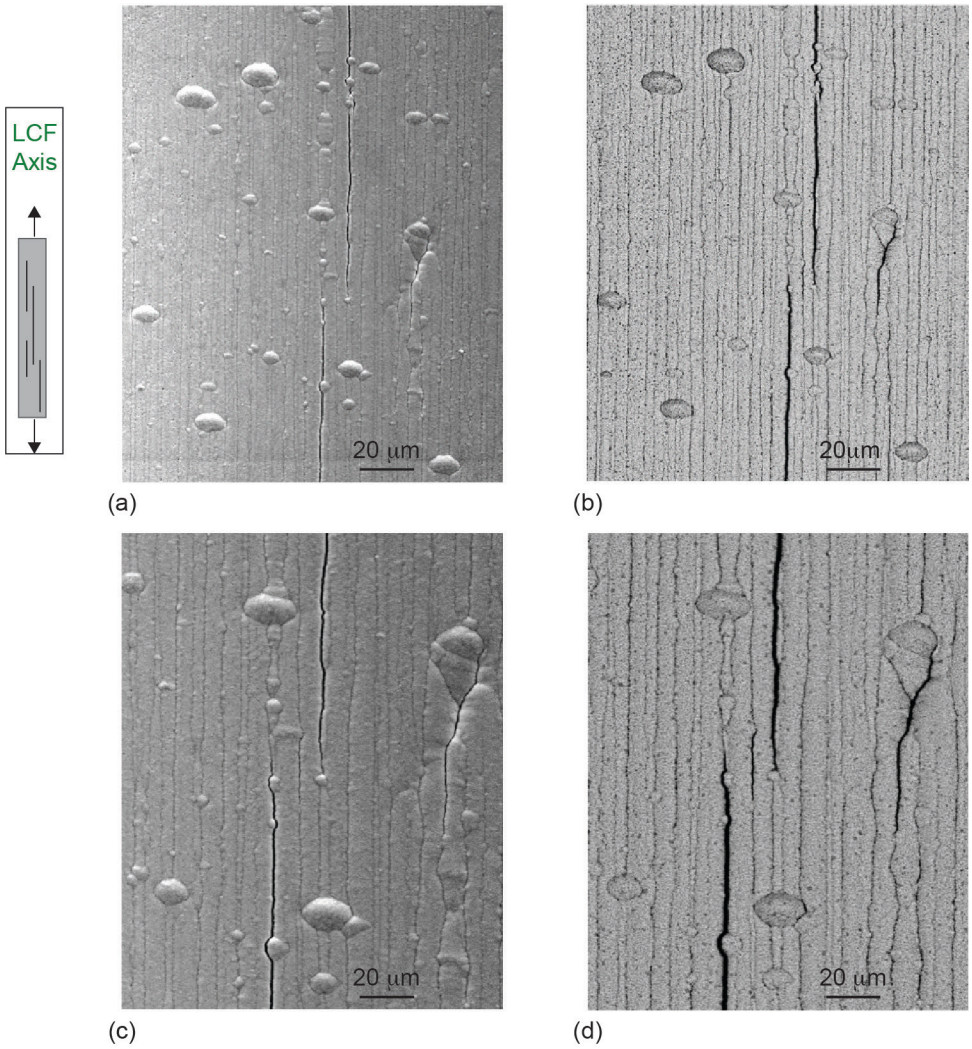

Figure 4.—Higher magnification (a,c) SEI and (b,d) BSE SEM images of the coating surface for the ***Low Cr***, ***Thin*** coating showing the "cracks" and coating texture oriented along the loading axis. The LCF loading axis is vertical for each of the images.

around the circumference, perpendicular to the pin axis. For these pins, the surface texture and the linear gaps were in the circumferential direction following the polishing marks. For growth of a typical thin sputtered coating (<1 μm thick), it would be expected that the coating morphology would follow that of the surface, however it was somewhat surprising to see the same fine texture of the substrate reflected in the surface of such a thick (~20 μm) coating.

The spits, as is commonly observed, did not appear to be well bonded to the surrounding coating and later processing indicated that they were sometimes dislodged and lost from the coating. Figure 5(a) shows a linear gap passing around a spit indicating a weak bond with the coating. A linear gap passing at the edge of a spit, shown in Figure 5(b), shows little interaction between the spit and the linear gap. The spits were not uniformly located across the specimen surface. Varying densities of spits on the surface are shown in Figure 5(c) and (d). For environmental protection (oxidation and hot corrosion), both the linear gaps and the weak interface at the spits were a concern, especially if loss of a spit during later processing could expose the substrate to corrosive reactants. Since the linear gaps ran parallel to the specimen loading axis, it was not known if these defects would have a detrimental effect on the LCF life. Certainly any cracks or linear defects in an orientation perpendicular to the specimen loading axis would be a major concern.

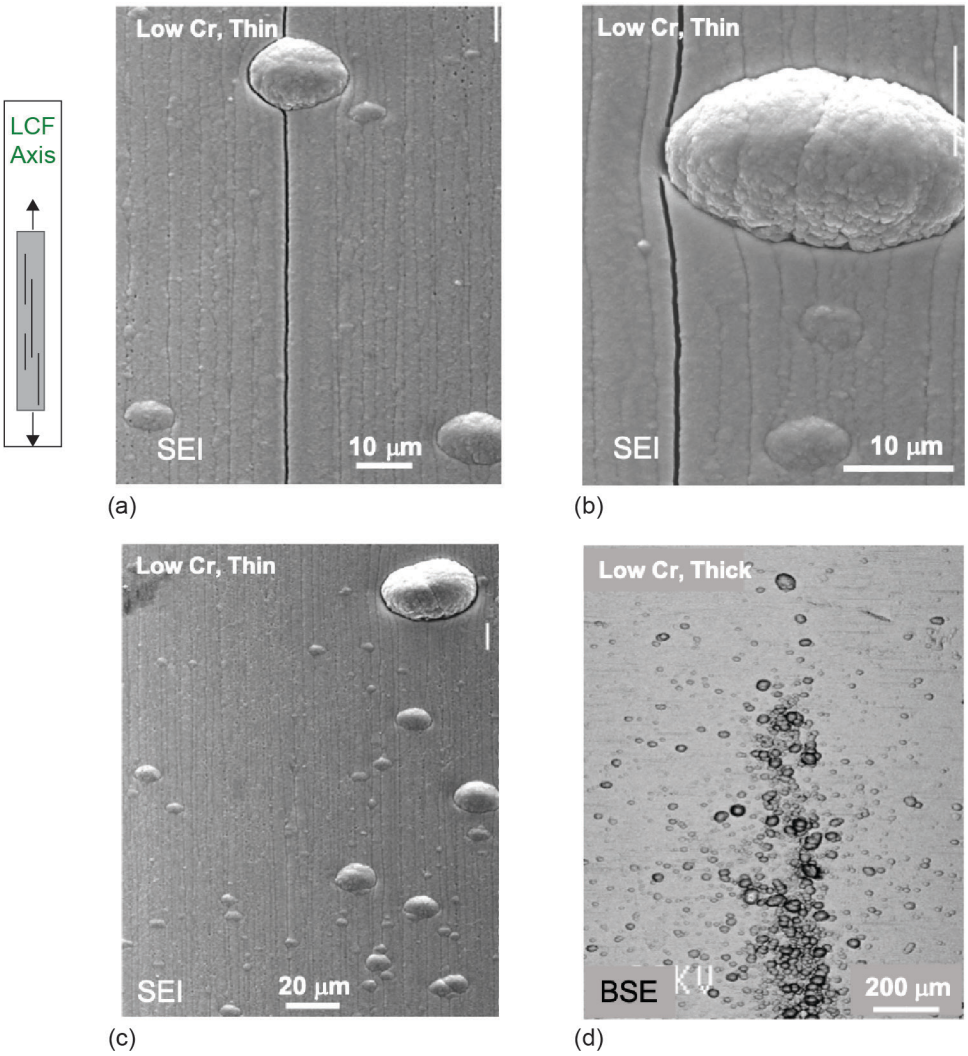

Figure 5.—SEM images (a,b) showing the linear gaps interacting with spits, and (c,d) showing the non-uniformity of spits on the surface. The LCF loading axis is vertical for each of the images. Coating ID's are shown in the upper left corner of each image.

Coating Microstructures

Representative polished cross-sections of the six coatings are shown in Figure 6. Unfortunately, cross-sections of the as-deposited coatings were not available, so the images shown are after an 8 hr low PO_2 diffusion anneal and LCF testing to failure, both at 760 °C. The total exposure time at 760 °C is noted in the lower left corner of each image. Images are arranged according to Cr concentration at the same approximate thickness in Figure 6(a) to (c) with the thicker coatings shown in Figure 6(d) and (e). Hence, comparing Figure 6(a) and (d) shows the thickness variation for the low Cr concentration (29 %Cr) and the thickness variation at the intermediate Cr composition (35 to 37 %Cr) in Figure 6(b) and (e). The Ni-35Cr coating with the thin ZrO_2 outer layer (***Med Cr+ZrO₂***, ***Thin***), which was also the thinnest overall coating, is shown in Figure 6(f). The darker appearance of the ***High Cr***, ***Thin*** coating (44 %Cr) is due to the presence of a second phase (Figure 6(c)). Because these views are perpendicular to the LCF specimen axis, the linear gaps, which mirror the polishing marks along the pin axis, are apparent in most of the coatings. Some of these linear gaps intersect the surface while others appear to initiate at the coating/substrate interface or appear within the coating and indicate the columnar growth of the coating.

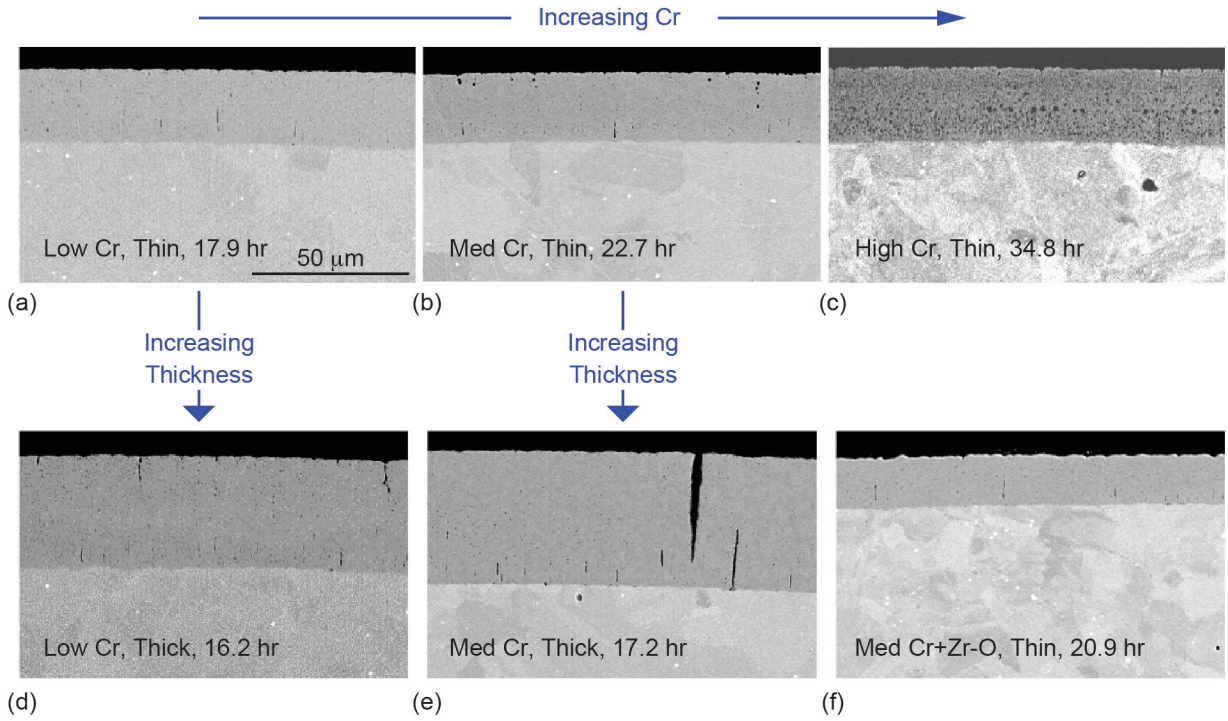

Figure 6.—SEM images of polished cross-sections for each of the coatings after the 8 hr, 760 °C low PO_2 diffusion anneal and LCF testing. The total time at 760 °C, including the 8 hr diffusion anneal and the LCF testing, is shown with the coating ID in the lower left of each image. The section was made perpendicular to the LCF loading axis away from the fracture surface. The micron marker shown in (a) applies for each image.

The second phase particles in the ***High Cr***, ***Thin*** coating are shown more clearly in Figure 7(a) and (d). EDS analysis (Figure 7(b)) showed these particles to be very high in Cr and are the BCC α-Cr phase (Ref. 16). The phase diagram (Ref. 77) shown in Figure 7(c) shows a relatively good match between the expected Cr concentration of the γ FCC matrix phase and that measured using EDS. It is somewhat surprising that the α-Cr particles are somewhat larger in the inner half of the coating (Figure 7(a) and (d)). A spit, which penetrates over a third of the coating depth, is also evident in Figure 7(d). The α-Cr phase was also observed at a much lower volume fraction in the ***Med Cr*** coatings, as shown in Figure 8(a) and (b) and a slightly lower volume fraction of this phase was observed in the ***Low Cr*** coating (Figure 8(c) and (d)). Although particles were distributed throughout the ***Low Cr*** coating, it was somewhat surprising to see a slightly higher volume fraction near the outer surface, with particles at, or within microns of the surface (Figure 8(d)). Oxidation at the surface would be expected to selectively form Cr_2O_3 and reduce the near-surface Cr concentration and result in a layer depleted of the high-Cr α phase. Perhaps because of the relatively short exposure time (~18 hr at 760 °C), there was little consumption of Cr in the coating. The α-phase recession after 500 hr oxidation will be clearly shown in a companion study (Ref. 78).

The thin Zr-O layer on the ***Med Cr-ZrO$_2$***, ***Thin*** coating is shown in Figure 9(a) to (c). EDS analysis of the outer layer showed a high Zr and O concentration and was likely ZrO_{2-x} where the x indicates the possibility of some oxygen deficiency. There was a very thin, dark layer of Cr-rich oxide below the ZrO_2 layer. It is not known if this layer formed during deposition of the Zr, or by oxygen transport through the ZrO_2 layer during the low PO_2 anneal or during LCF testing. Cr-rich oxide was apparent in one of the linear gaps that intersected the surface. The cusps bordering the top of this gap further suggest that these linear gaps develop during growth of the Ni-35Cr-Y coating and not by some fracture or cracking of the coating following coating deposition. The Cr_2O_3 formation in the gap (Figure 9(c)) may have formed as a result of excess oxidation during the deposition of the ZrO_2 layer or during the 8 hr low PO_2 diffusion anneal.

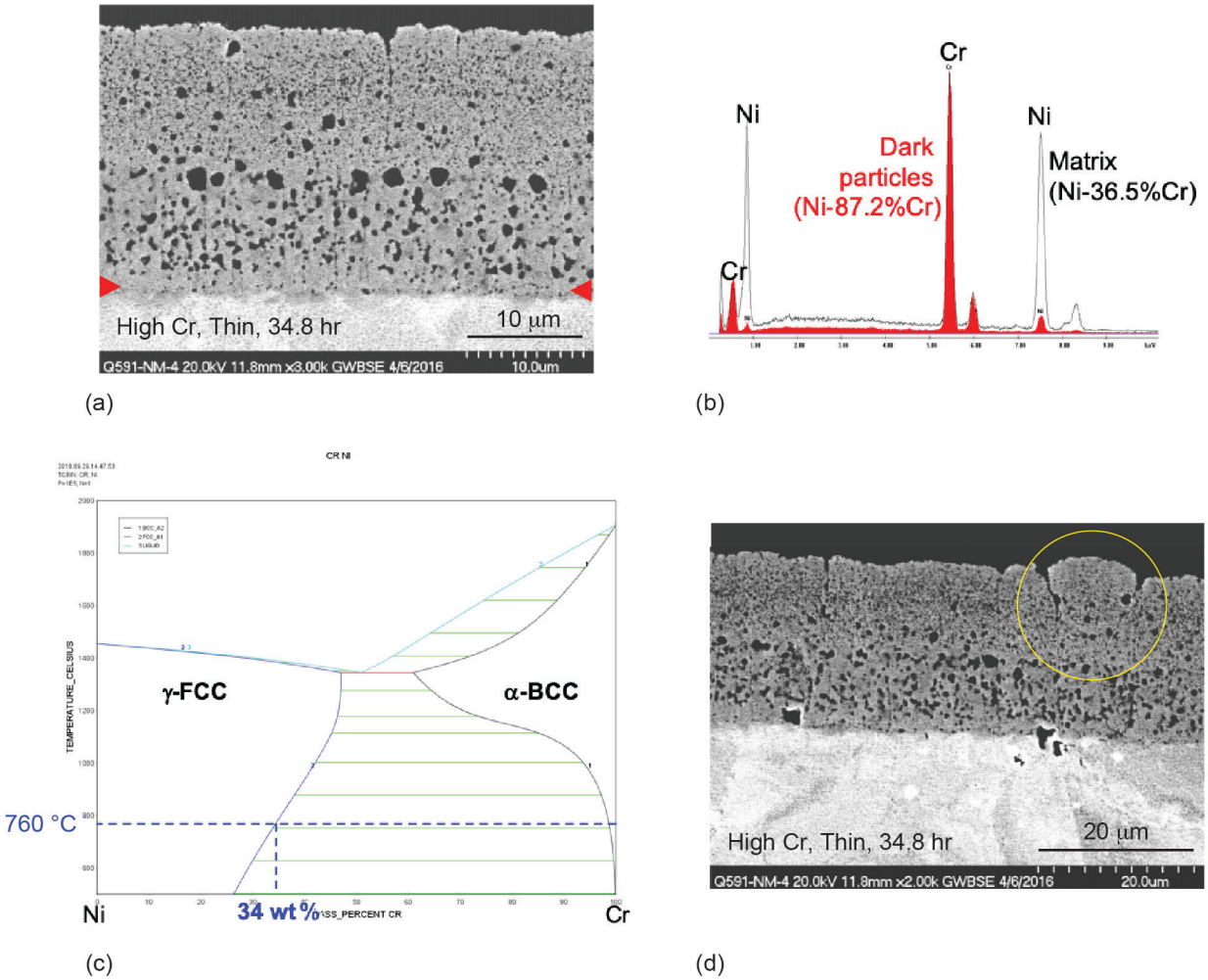

Figure 7.—(a) BSE image of the ***High Cr***, ***Thin*** coating showing the second-phase particles (dark). (b) Comparison of EDS spectra, normalized to the same Cr peak height, and ZAF analysis results showing that the dark particles are high in Cr (~87%) while the matrix is ~36 %Cr. (c). Ni-Cr phase diagram showing that the high-Cr particles are the BCC α-Cr phase and the Cr concentration in the γ-FCC matrix phase is ~34 wt. (d). Image showing a spit (circled) and the uneven distribution of the α particles.

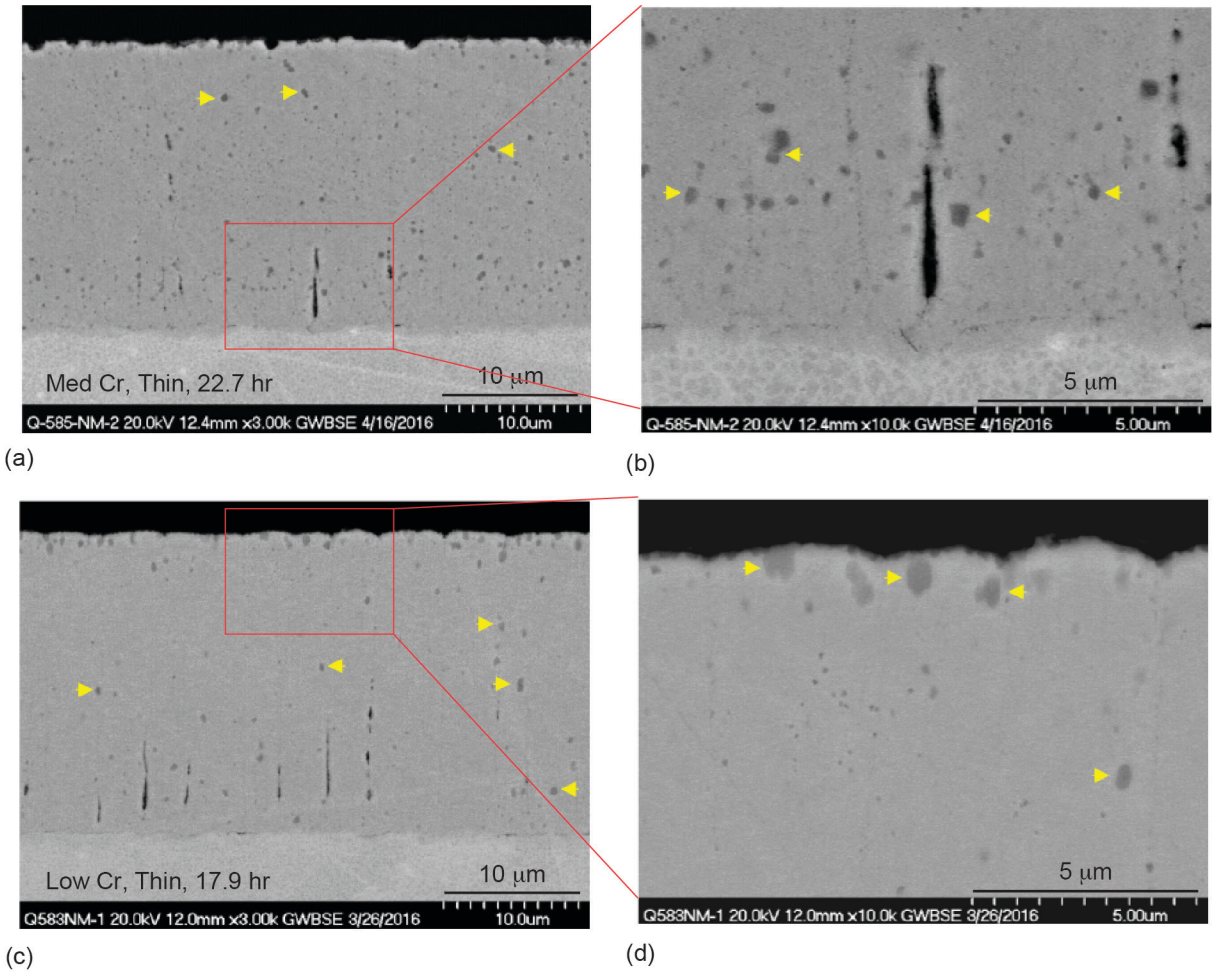

Figure 8.—BSE images showing the second phase α-Cr particles (medium gray) distributed throughout the (a,b) ***Med Cr***, ***Thin*** coating, and (c,d) ***Low Cr***, ***Thin*** coating. Yellow arrows indicate the location of some of the particles. (b,d) Magnified views of the red boxes shown in (a,c), respectively. The total time at 760 °C, including the 8 hr diffusion anneal and the LCF testing, is shown with the coating ID in the lower left of images (a,c).

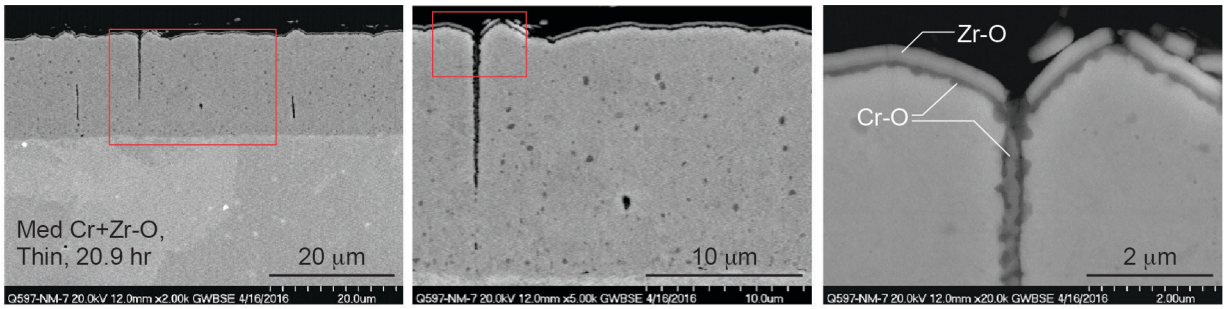

Figure 9.—(a-c) BSE images of the ***Med Cr+Zr-O***, ***Thin*** coating showing progressively higher magnifications of the thin Zr-O layer and one of the linear gap defects which contains some Cr-rich oxide. There is also the indication of a Cr-rich oxide (thin dark layer) below the Zr-rich layer.

There were many other coating defects observed in these coatings. Some of the linear gaps were observed to penetrate to the substrate (Figure 10(a)). Spits were observed at the surface as well as interior to the coating (Figure 10(b)), and on the ***High Cr***, ***Thin*** coating regions were observed where the coating appeared missing/lost (Figure 10(c)). The ***Med Cr***, ***Thick*** coating showed regions with large numbers of wide linear gaps (Figure 10(d)).

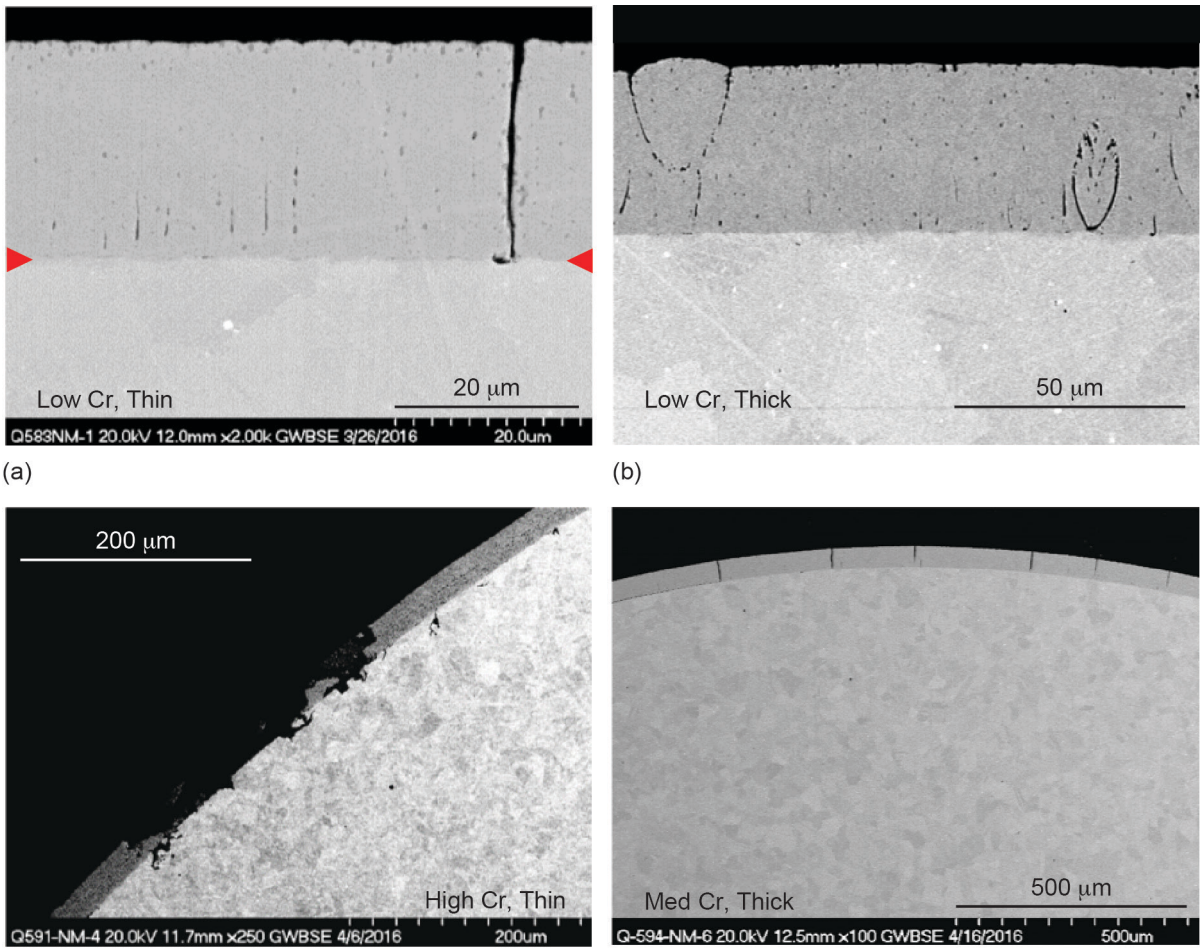

Figure 10.—(a-d) BSE images showing various defects observed on several of the samples. LCF specimens were sectioned after the 8 hr low PO_2 diffusion anneal and LCF testing. The section was made perpendicular to the LCF loading axis away from the fracture surface.

LCF Testing

LCF testing at 760 °C was performed on LSHR-coated specimens with each of the coatings, and comparisons were made by testing the ME3 substrates with the ***Low Cr***, ***Thin*** coating. All coated LCF specimens were tested after receiving the 8 hr low PO_2 diffusion anneal. For further comparisons, uncoated LSHR specimens were also tested under the same LCF test conditions but without the 8 hr low PO_2 anneal. The fatigue life results for the coated and uncoated specimens are shown in Figure 11. The LCF lives for each specimen are given in Table 3 as well as the total time at 760 °C for each specimen which includes the time during LCF testing as well as the 8 hr diffusion anneal for the coated specimens. Clearly, in comparison to the uncoated specimens, applying the coatings and giving the 8 hr low PO_2 diffusion anneal degraded the LCF life of the coated disk alloy. The ***High Cr***, ***Thin*** coating showed the best LCF life whereas the ***Low Cr***, ***Thick*** coatings yielded the lowest LCF life. There was no significant difference in the LCF life between the LSHR and ME3 substrates coated with the ***Low Cr***, ***Thin*** coating. Clearly, the LCF life increased with Cr content for the thin coatings. Although the LCF lives were lowest for the thick coatings, the lives also increased slightly from the ***Low Cr*** to the ***Med Cr*** samples. The addition of the ZrO_2 top layer to the ***Med Cr***, ***Thin*** coating had little effect on the LCF life, as seen by comparing the ***Med Cr***, ***Thin*** coatings to the ***Med Cr+ZrO₂***, ***Thin*** coatings. It should be noted that although the uncoated specimens did not receive the 8 hr low PO_2 diffusion anneal, time at 760 °C for the specimens was similar when the time of LCF testing at 760 °C was taken into account, as shown in the "Total Time at 760 °C" column in Table 3. Hence, it is unlikely that the 8 hr low PO_2 anneal given only to the coated specimens significantly degraded the LCF life of those coatings.

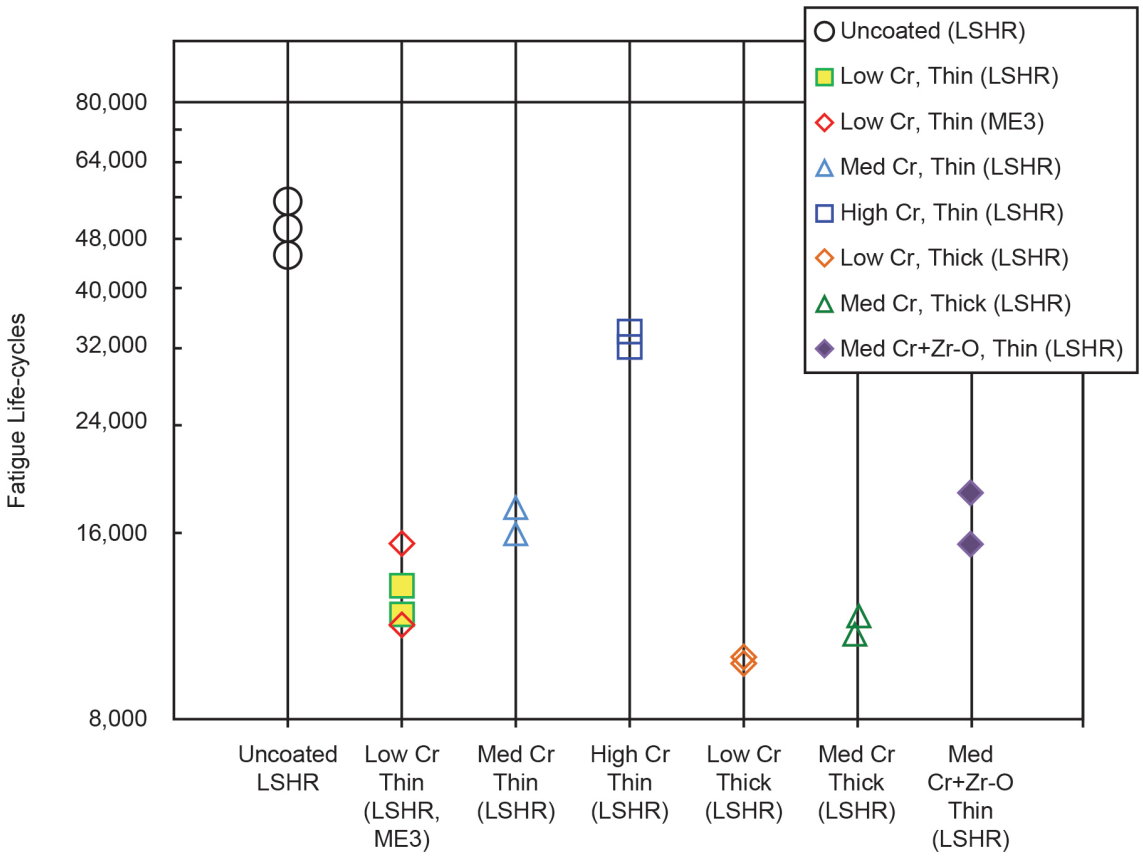

Figure 11.—LCF life for the uncoated and coated specimens. The coated specimens were tested after the low PO_2 treatment. Note the logarithmic scale.

TABLE 3.—ALLOY, COATING DESIGNATION, CR CONTENT, THICKNESS AND LCF LIFE, TOTAL TIME AT 760 °C

Alloy	Coating designation	Cr content, wt%[a]	Coating thickness, μm[b]	LCF life, cycles	LCF test time, hr[c]	Total time at 760 °C, hr[d]
LSHR	Uncoated[e]	----	---	55,123	45.9	45.9
LSHR	Uncoated[e]	----	---	46,025	38.4	38.4
LSHR	Uncoated[e]	----	---	49,879	41.6	41.6
LSHR	***Low Cr***, ***Thin***	29	20	11,833	9.9	17.9
LSHR	***Low Cr***, ***Thin***	29	20	13,201	11.0	19.0
ME3	***Low Cr***, ***Thin***	29	20	11,362	9.5	17.5
ME3	***Low Cr***, ***Thin***	29	20	15,371	12.8	20.8
LSHR	***Med Cr***, ***Thin***	37.0	21	17,648	14.7	22.7
LSHR	***Med Cr***, ***Thin***	37.0	21	16,039	13.4	21.4
LSHR	***High Cr***, ***Thin***	44	20	32,161	26.8	34.8
LSHR	***High Cr***, ***Thin***	44	20	33,979	28.3	36.3
LSHR	***Low Cr***, ***Thick***	29	38	9,878	8.2	16.2
LSHR	***Low Cr***, ***Thick***	29	38	10,090	8.4	16.4
LSHR	***Med Cr***, ***Thick***	35	41	11,000	9.2	17.2
LSHR	***Med Cr***, ***Thick***	35	41	11,755	9.8	17.8
LSHR	***Med Cr+ZrO_2***, ***Thin***	35	19	15,452	12.9	20.9
LSHR	***Med Cr+ZrO_2***, ***Thin***	35	19	18,600	15.5	23.5

[a]Composition measured by EDS

[b]Thickness measured on pins after 16N-200 percent shot peen and 8 hr low PO_2 diffusion anneal

[c]Total time at 760 °C during LCF testing

[d]Total time at 760 °C including 8 hr diffusion anneal

[e]Uncoated specimens did not receive the 8 hr diffusion anneal

Fracture and Coating Surfaces

Following the LCF testing, failure initiation sites were identified for each failed specimen. For these specimens, crack initiation sites were relatively easy to identify optically at relatively low magnifications, as shown in Figure 12. In both specimens shown in this figure, failures were initiated by a single crack identified as the primary failure crack. The initiation site for this crack is indicated by the yellow triangle in the figure. However, in Figure 12(b), several other secondary cracks (red triangles) had obviously initiated at different locations in addition to the primary failure crack. SEM was used to follow typical crack growth patterns for fatigue failures to identify and examine the initiation site of the primary failure crack. The intent was to identify whether the crack initiated at the surface, or at an internal flaw within the substrate. The failure initiation site of one of the ***Low Cr***, ***Thin*** coated specimen is shown in Figure 13. The initiation site for this specimen was at the surface. A closer examination of the site indicated the presence of two spits in the coating, which are seen to penetrate nearly through the coating (Figure 13(c)). It is likely that these spits initiated the fatigue crack which grew to become the primary failure crack.

After identifying the crack initiation site for the primary failure crack, the specimen was rotated and the coated surface of the specimen was also examined in the region where the primary failure crack initiated. Although linear gaps parallel to the loading axis were observed after coating (Figure 3 and Figure 4), numerous fatigue cracks perpendicular to the loading axis can also be seen in Figure 14. A closer examination indicated that most of these cracks are associated with large and small spits (Figure 14(b) to (d). Hence, based on Figure 13 and Figure 14, it appears that for this specimen, fatigue cracks initiated at spits in the coating with one crack propagating into the substrate as the primary failure crack. However, for a small number of specimens, one of the longitudinal linear gaps appeared to be the primary crack initiation site, as shown in Figure 15. A close examination of Figure 15(b) shows that this linear gap extended through the coating to the substrate. Because these linear gaps are parallel to the loading axis, they were not expected to significantly contribute to the perpendicular fatigue crack growth but may have

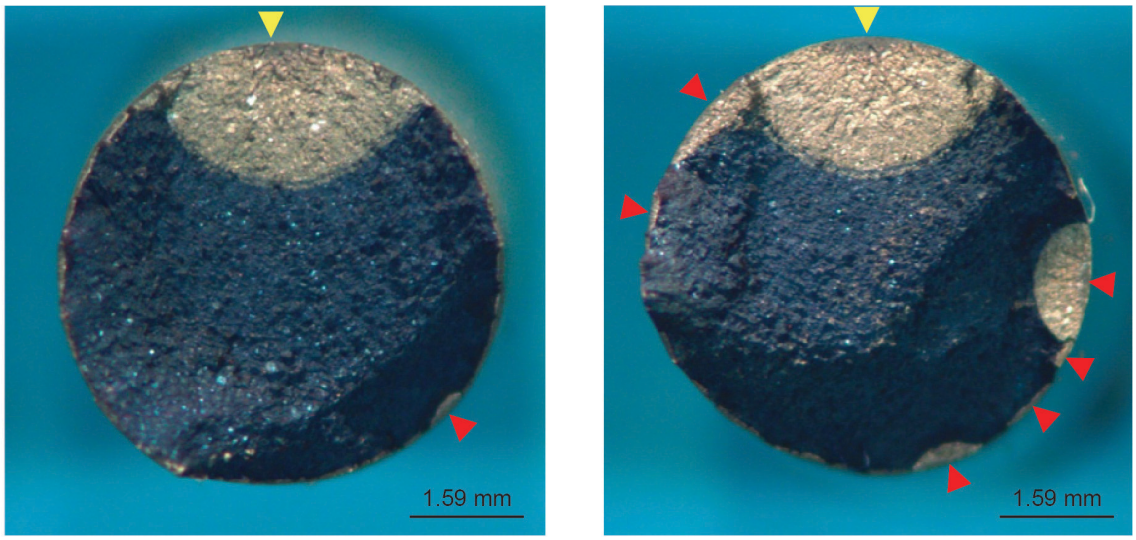

(a) (b)

Figure 12.—a,b. Optical images of the fracture surfaces after LCF testing showing crack initiation sites with the primary failure crack initiation site oriented to be at the top (yellow triangle). Other significant cracks are indicated with red triangles.

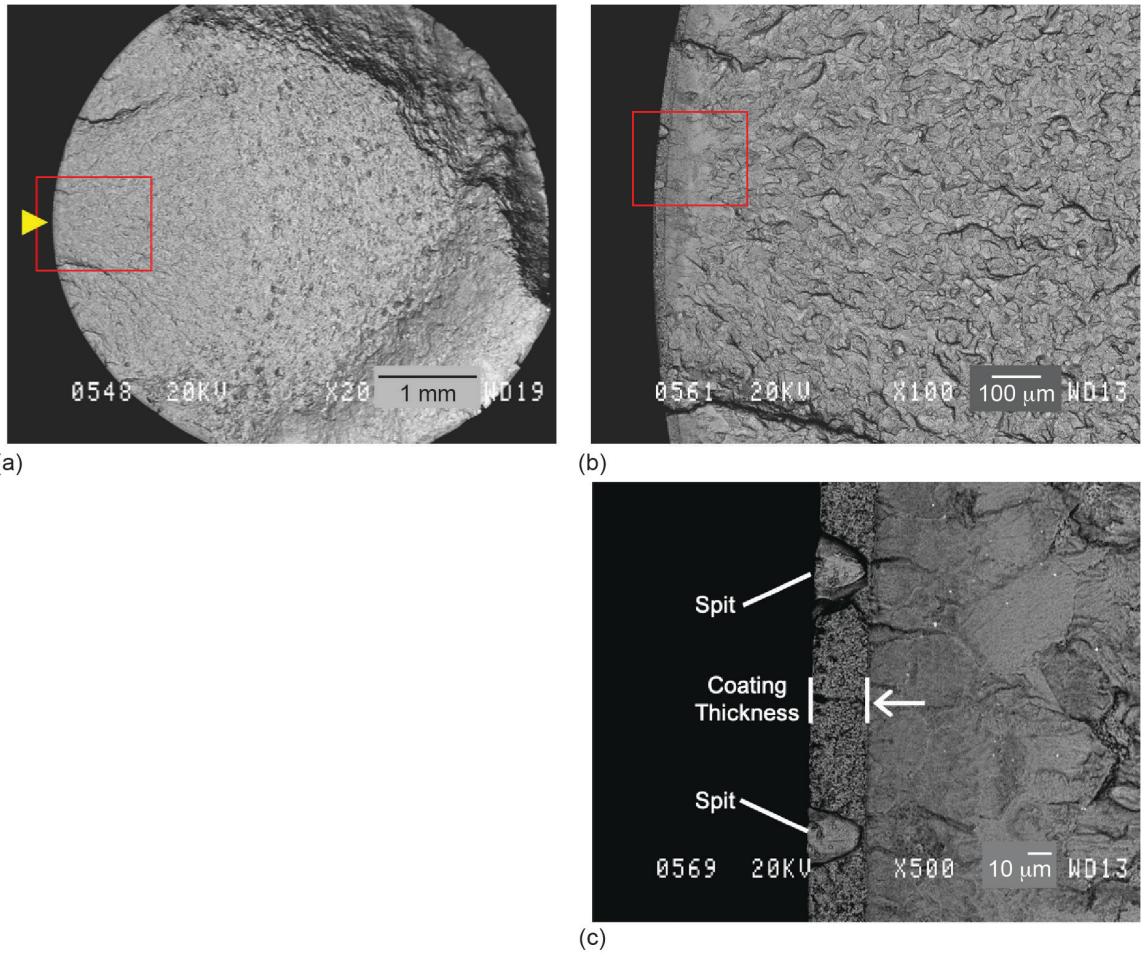

(a) (b) (c)

Figure 13.—BSE images of the fracture surface showing the crack initiation site (yellow triangle). Clearly visible in (c) is the location of two spits in the coating which appear to penetrate most of the coating. (***Low Cr***, ***Thin*** coating).

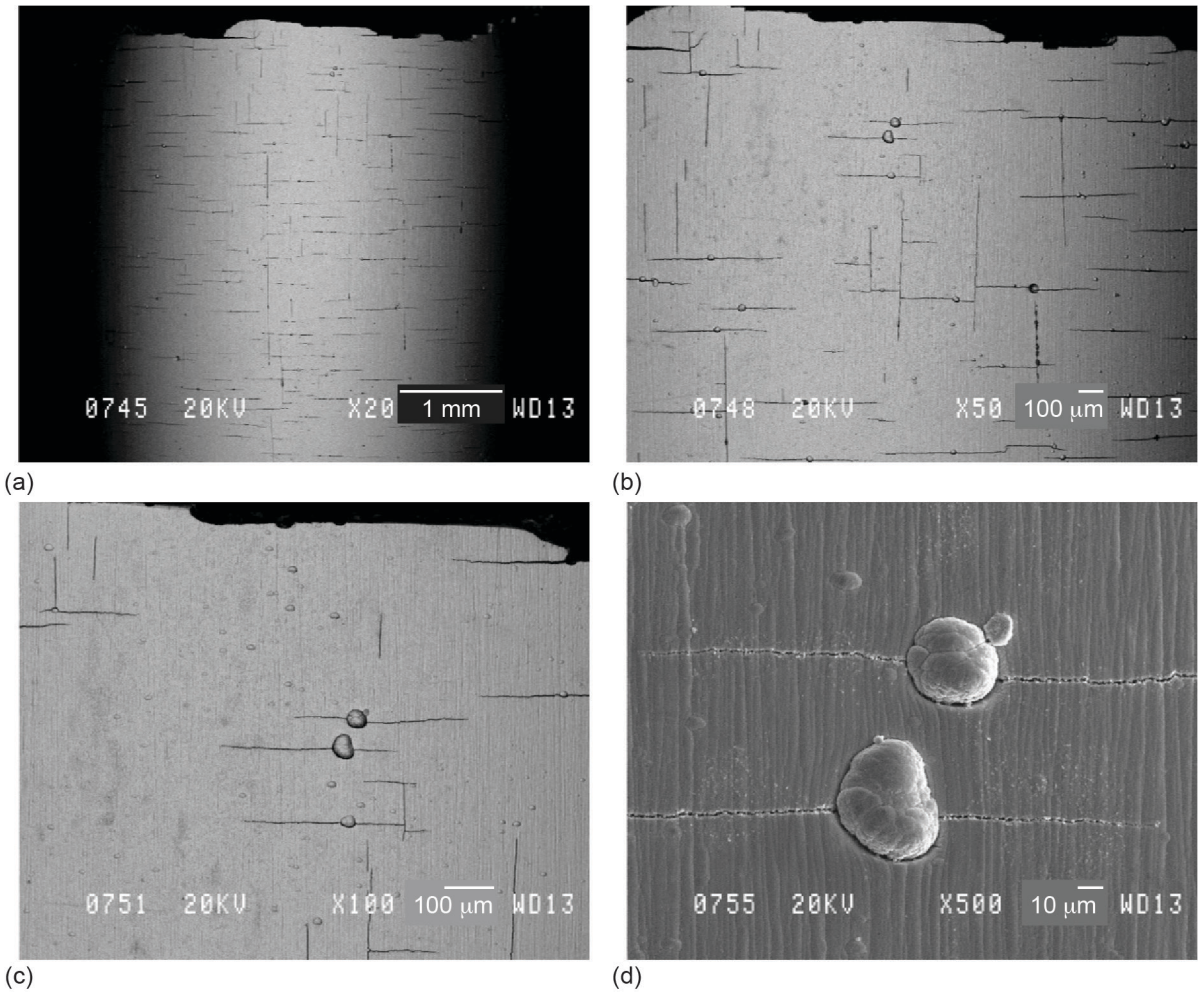

Figure 14.—BSE (a-c) images of the surface of the LCF specimen after testing showing the formation of cracks parallel and perpendicular to the LCF loading axis. (d) SEI image showing cracks associated with two spits. (***Low Cr***, ***Thin*** coating).

precipitated crack initiation of a perpendicular fatigue crack, as suggested in Figure 15. However, it is not certain whether the linear gap initiated the primary fatigue crack, or was simply present near the primary crack initiation site. EDS of the specimen gage surfaces indicated elevated Cr and O levels, consistent with the formation of principally chrome oxide on both uncoated and coated specimen surfaces.

For the ***Low Cr***, ***Thin***, ***Low Cr***, ***Thick***, and ***Med Cr+ZrO_2***, ***Thin*** specimens, spits were clearly identified at the primary crack initiation sites, similar to that shown in Figure 13. For the ***Med Cr***, ***Thin*** and ***Med Cr***, ***Thick*** specimens, linear gaps parallel to the loading axis were apparent at the primary crack initiation sites. Each of the specimens had obvious fatigue cracks on the surface perpendicular to the loading axis, similar to those seen in Figure 14(b) and Figure 15(c). Many of these perpendicular fatigue cracks were associated with a spit on the surface, as shown in Figure 13 and Figure 14. Unlike the other coatings, the ***Med Cr***, ***Thick*** coating showed a gap between the coating and substrate in views of the fracture surface (Figure 16(a)) and evidence of a poor bond between the coating and substrate near the site of the primary crack initiation (Figure 16(b)). On the side of the gage section, there were large numbers of longitudinal cracks in the coating running parallel to the loading axis as well as the expected fatigue cracks running perpendicular to this axis (Figure 16(c)). Cracks both parallel and perpendicular to the loading axis appeared longer and wider for this coating. In contrast to the extensive surface cracks for

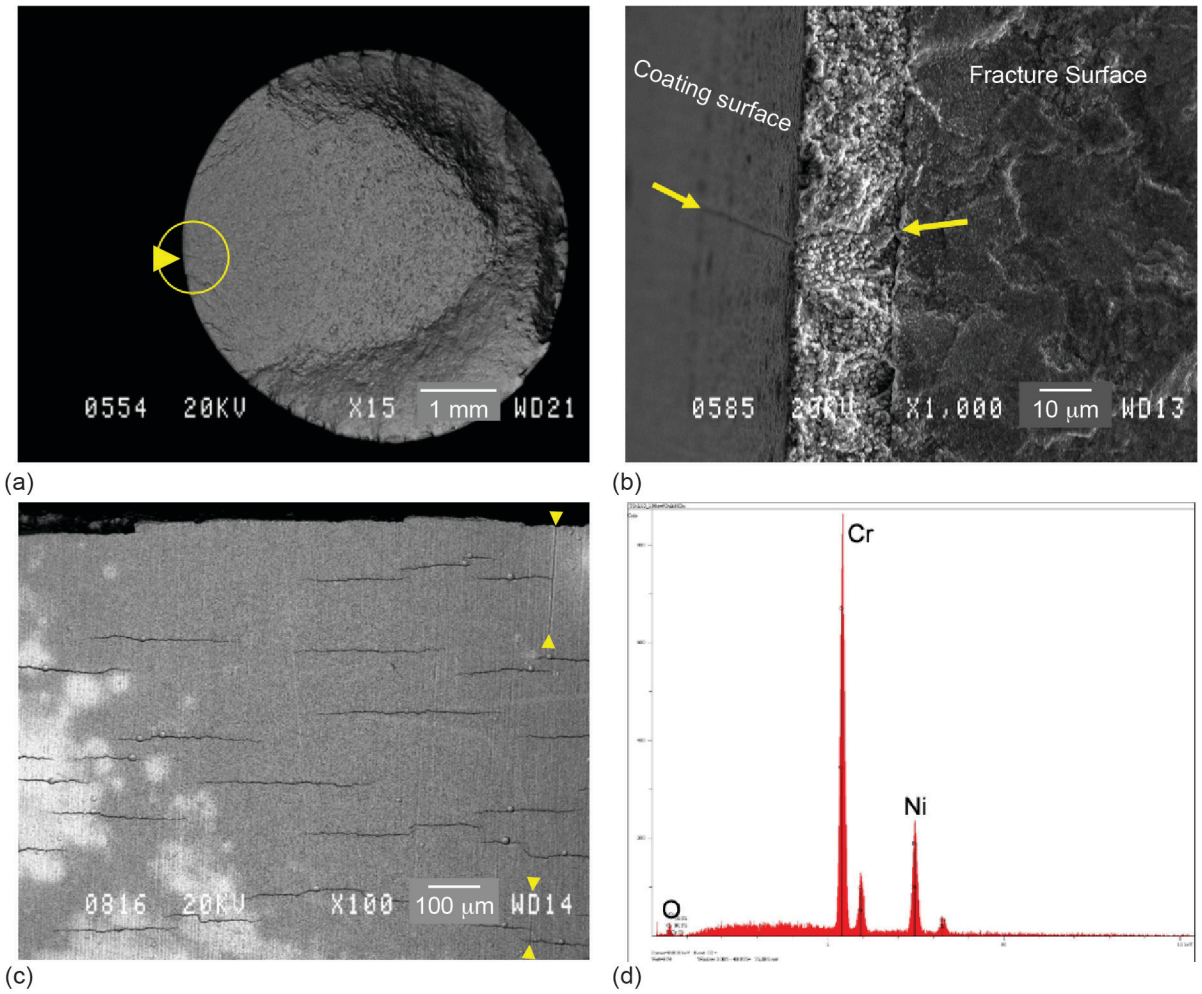

Figure 15.—BSE (a,c) and SE (b) images of the fracture surface of the LCF specimen showing the site of crack initiation at a linear gap parallel to the loading axis which has penetrated through the coating (see arrows in (b)). Fatigue cracks perpendicular to the loading axis are shown in (c) where two of the linear gaps parallel to the loading axis (vertical in the image) are highlighted by the yellow arrows. An EDS spectra (d) of the surface in (c) shows that the surface oxide is high in Cr. (***Med Cr***, ***Thin*** coating).

the ***Med Cr***, ***Thick*** coating, far fewer perpendicular fatigue cracks were observed with the ***Med Cr+ZrO$_2$***, ***Thin*** coating (Figure 17). This thin, two-layer coating again mirrored the pattern of the longitudinal polishing marks on the LCF specimen (Figure 17(b)). Fine, linear gaps (vertical in the image) were present but could only be discerned at higher magnification (see yellow arrowheads in Figure 17(b)).

For the two specimens with the ***High Cr***, ***Thin*** coating, which exhibited the highest LCF lives of the coated specimens, a spit-like defect was observed in the coating at the primary crack initiation site in one of the specimens (Figure 18(a) and (b)) but no obvious spit or linear gap was observed in the second specimen. Examination of the coated sides of both specimens showed an unusually high number of perpendicular fatigue cracks (Figure 18(c) and (d)). In the one specimen (Figure 18(c)), the cracks appear much wider than for other specimens. Since these two specimens experienced nearly twice the number of fatigue cycles as other specimens, the high number of fatigue cracks may be related to this higher number of cycles. However, it may be that the ***High Cr*** coating has a higher propensity for developing fatigue cracks.

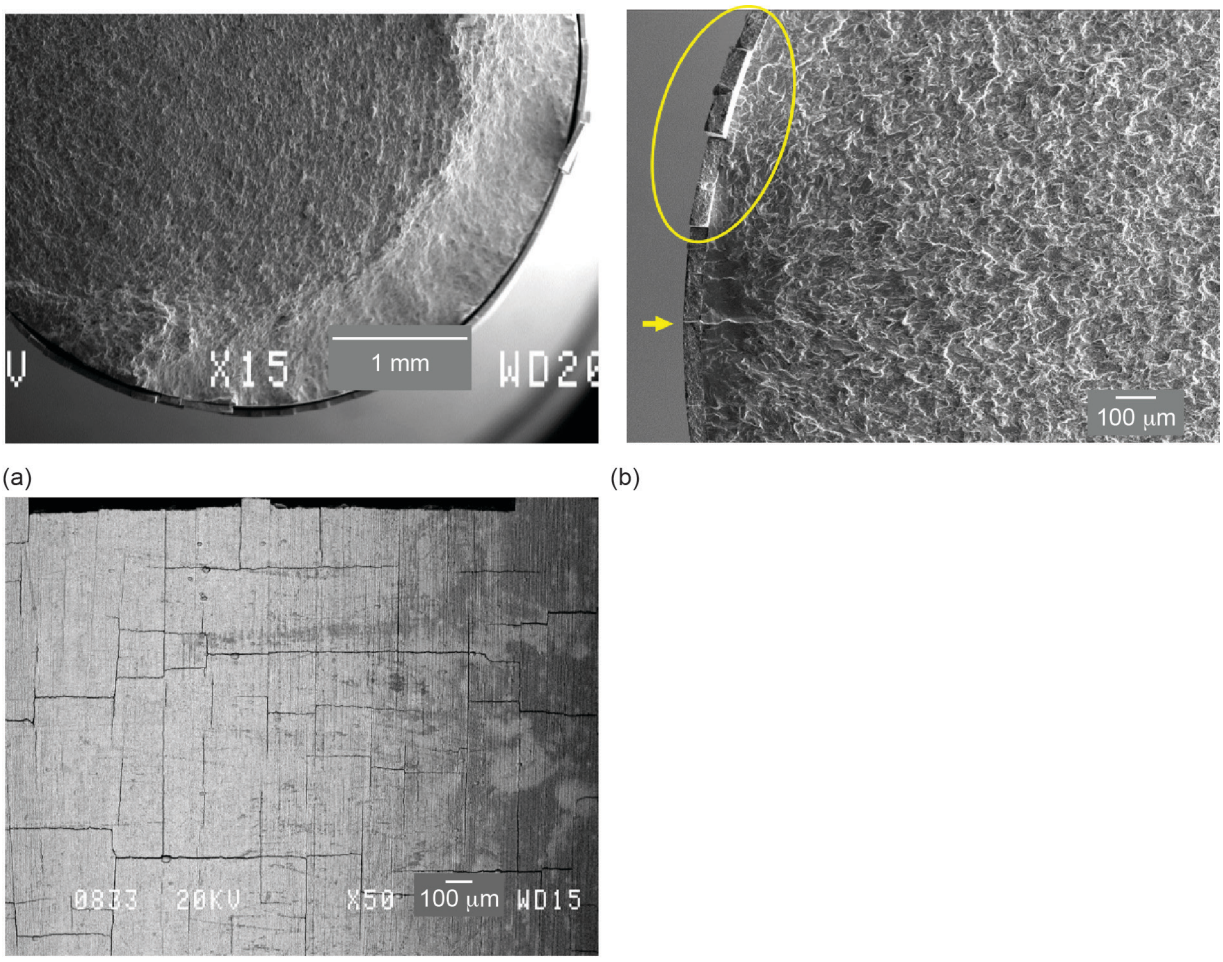

(a) (b)

(c)

Figure 16.—SE images of the fracture surface of the ***Med Cr***, ***Thick*** coated specimen showing (a) a gap between the coating and substrate, and (b) coating sections indicating a poor bond to the substrate (yellow oval) at a location near the crack initiation site (yellow arrow). (c) BSE image showing large numbers of longitudinal cracks parallel to the loading axis in addition to the expected perpendicular fatigue cracks.

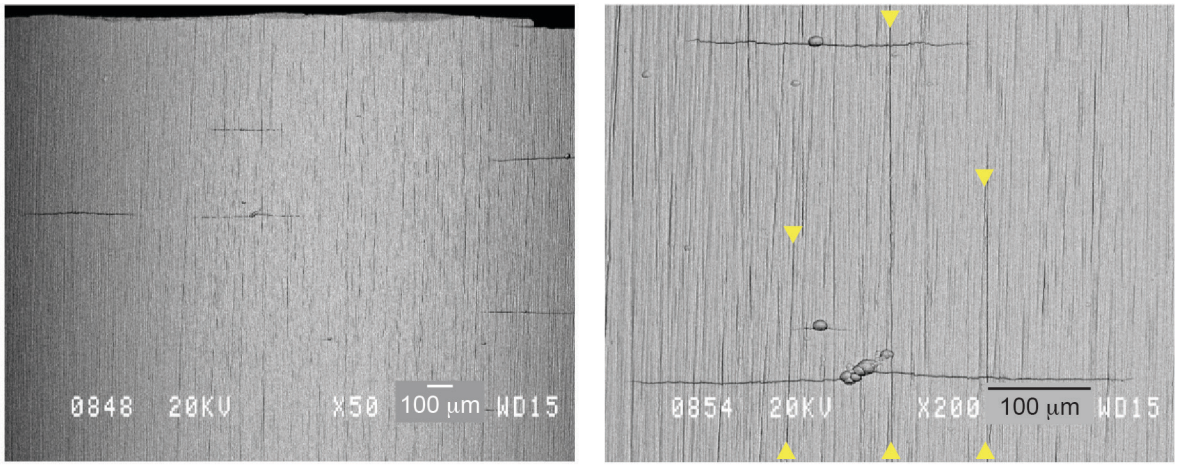

(a) (b)

Figure 17.—BSE images of the coated surface of the ***Med Cr+Zr-O***, ***Thin*** coating after LCF testing showing few spits, few perpendicular fatigue cracks, and fewer vertical (parallel to loading axis) cracks (indicated by the yellow arrowheads).

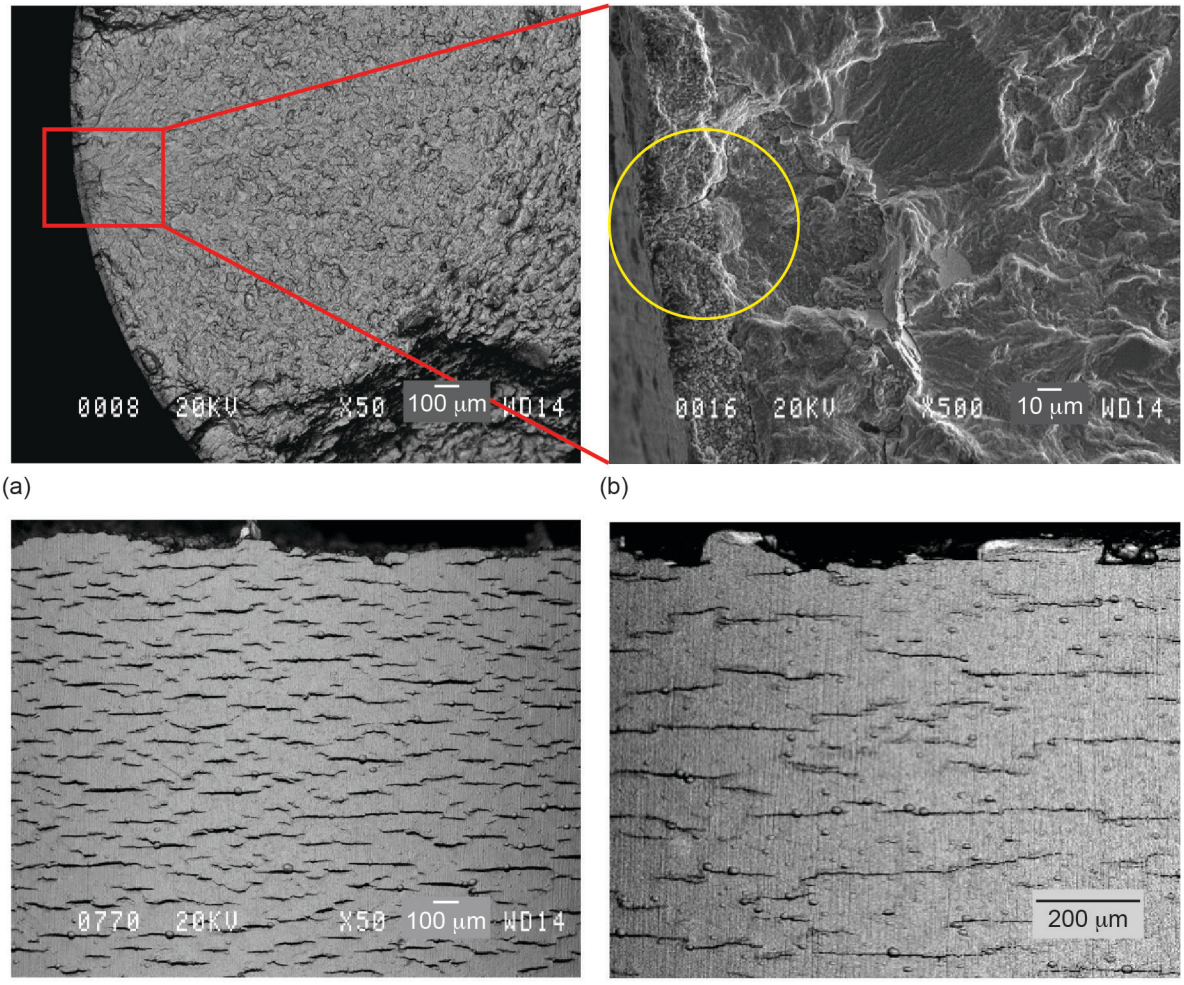

(a) (b)

(c) (d)

Figure 18.—BSE (a,c,d) and SE (b) images of the fracture surface and coated surface after LCF testing of the ***High Cr***, ***Thin*** coating. A defect in the coating (yellow circle in (b) was located at the primary crack initiation site. An unusually large number of perpendicular fatigue cracks are shown in (c,d) which were taken on different tested LCF specimens with the ***High Cr***, ***Thin*** coating. (Note the difference in magnification between (c) and (d).)

Uncoated Specimens

For comparison, the fracture surfaces of the three uncoated specimens were also examined, and the fracture surfaces of two specimens are shown in Figure 19(a) and (b). The primary crack initiation site for all three specimens was at the surface, similar to the coated specimens, although a second, smaller internally initiated site was observed for one of the specimens (circular area in Figure 19(b)). On the surface of the specimens, very small cracks were apparent which were easily identified by the growth of oxide protruding from the cracks (Figure 19(d) and (e)). Magnified views of the surface (Figure 20) shows that the oxide formation follows the pre-test texture of the longitudinal polishing lines aligned with the loading axis. This oxide formed during the LCF testing since it should be noted that the uncoated specimens received no low PO_2 diffusion anneal prior to testing. The hot exposure time at 760 °C for each of the uncoated specimens was 38.4 to 45.9 hr (Table 3). Because the oxide scale was relatively thin, EDS spectra of the overall surface at lower magnifications (e.g., Figure 19(d) and Figure 20(a)) generally reflected the overall alloy composition with somewhat enhanced peaks for Cr, Ti and Al (Figure 21(a)). EDS spectra of the somewhat thicker oxide at the cracks showed dominant peaks for Cr with enhanced peaks for Co or Ti (Figure 21(b)). It was unknown what role the fine, longitudinal polishing marks had, if any, in helping to initiate the fatigue cracks. The location of the primary failure crack initiation site for one of the specimens is indicated with the yellow arrowhead in Figure 22(a). The most distinguishable polishing marks in this image are indicated by red arrowheads and lie on either side, but not at the site of crack initiation suggesting the longitudinal polishing marks may play little or no role in the initiation of the primary failure crack. Magnified views of the surface show that small polishing marks are present across the surface and typically pass through most of the fatigue cracks. Hence, for the uncoated specimens, it is not expected that the fine polishing marks play any significant role in initiating the fatigue cracks.

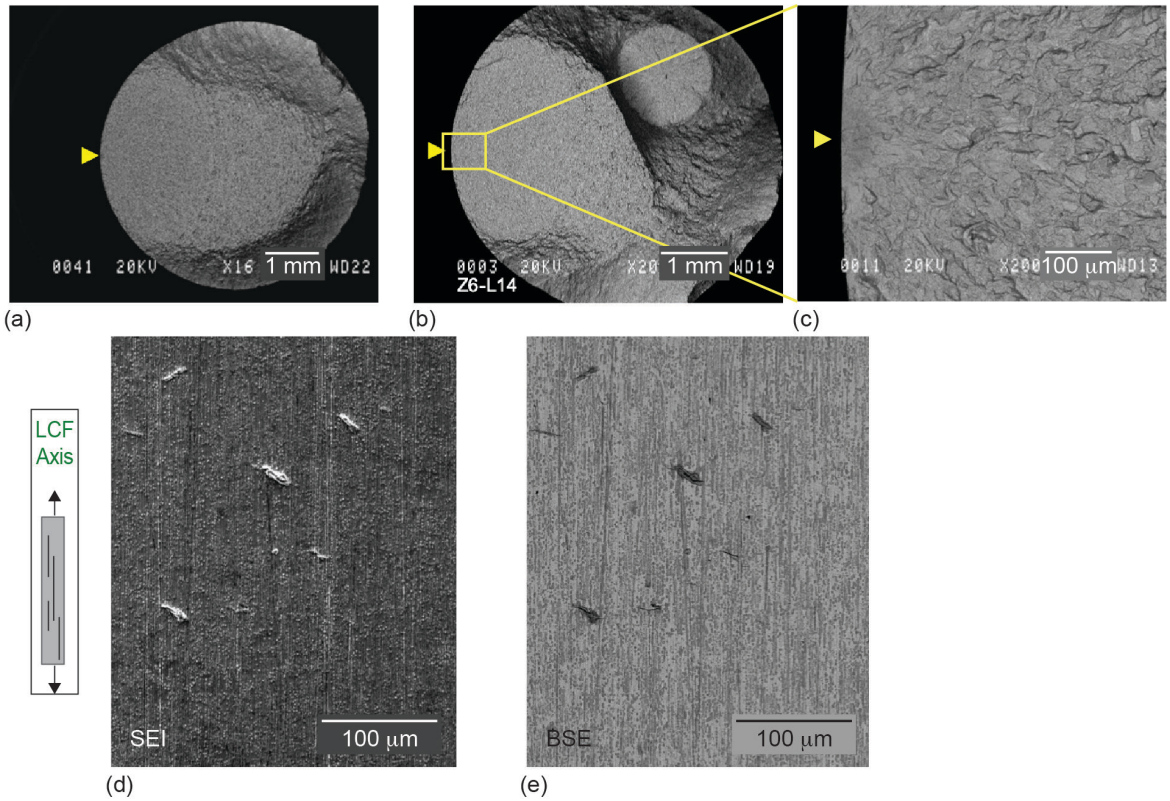

Figure 19.—BSE (a-c) images of the fracture surface of two of the uncoated specimens after LCF testing. The primary crack initiation site is indicated with yellow markers. Note the second, smaller internal initiation site in (b). SE (d) and (e) BSE images of the surface of the specimen near the primary crack initiation site showing oxide growths which identify cracks.

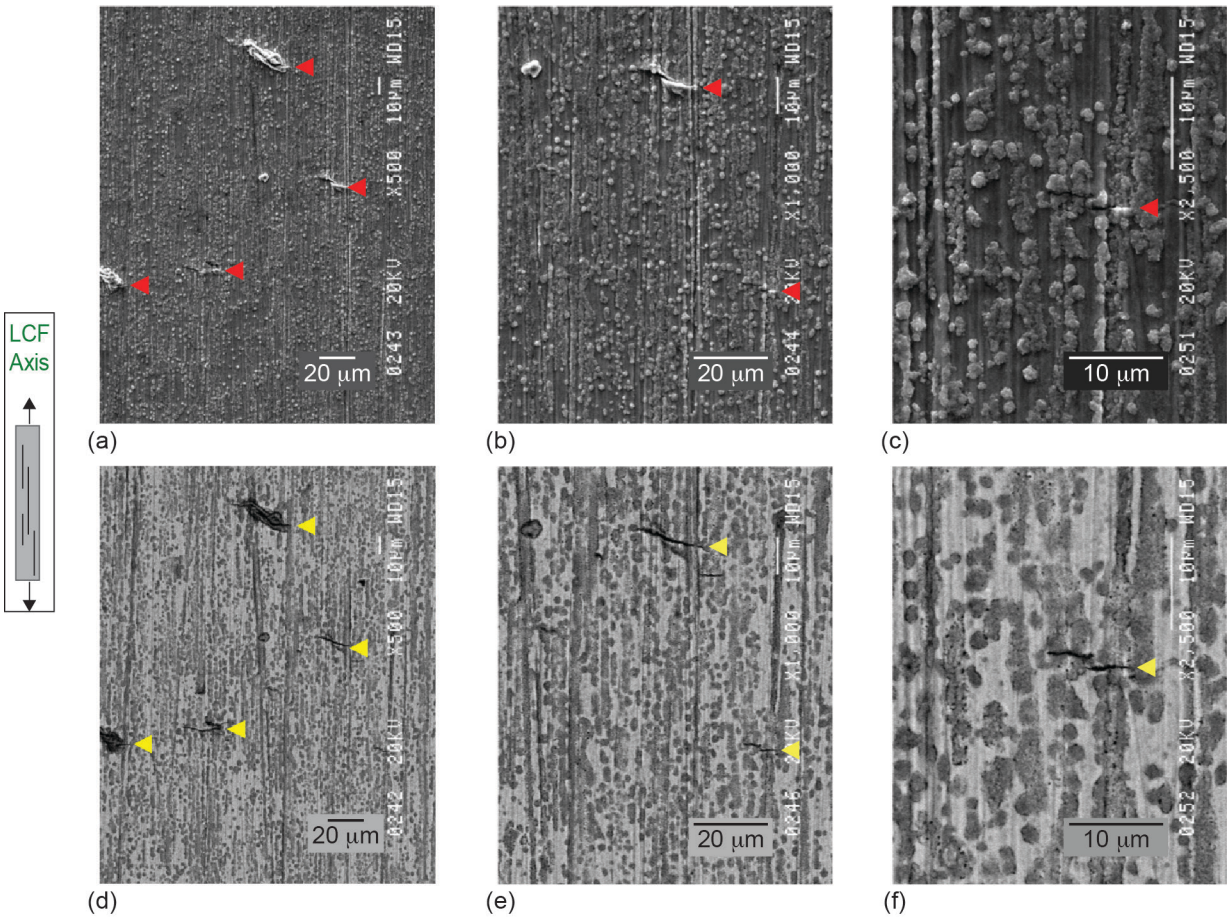

Figure 20.—SE (a-c) and BSE (d-f) images of the side of one the uncoated specimens after LCF testing. Oxide protrusions on the surface (red arrows in a,b) mark most of the cracks which are more apparent in the BSE images (yellow arrowheads in d-f). No oxide protrusion is evident for the smallest crack shown in (f). The oxide growths follow the texture of the pre-test longitudinal polishing lines (vertical in the figure).

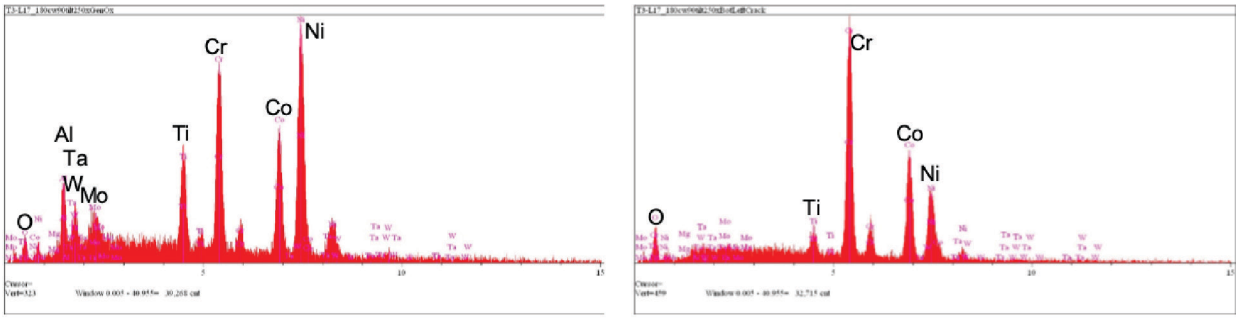

Figure 21.—EDS spectra for (a) the overall surface, and (b) a typical spectra for the Cr-rich oxide protrusions at the cracks.

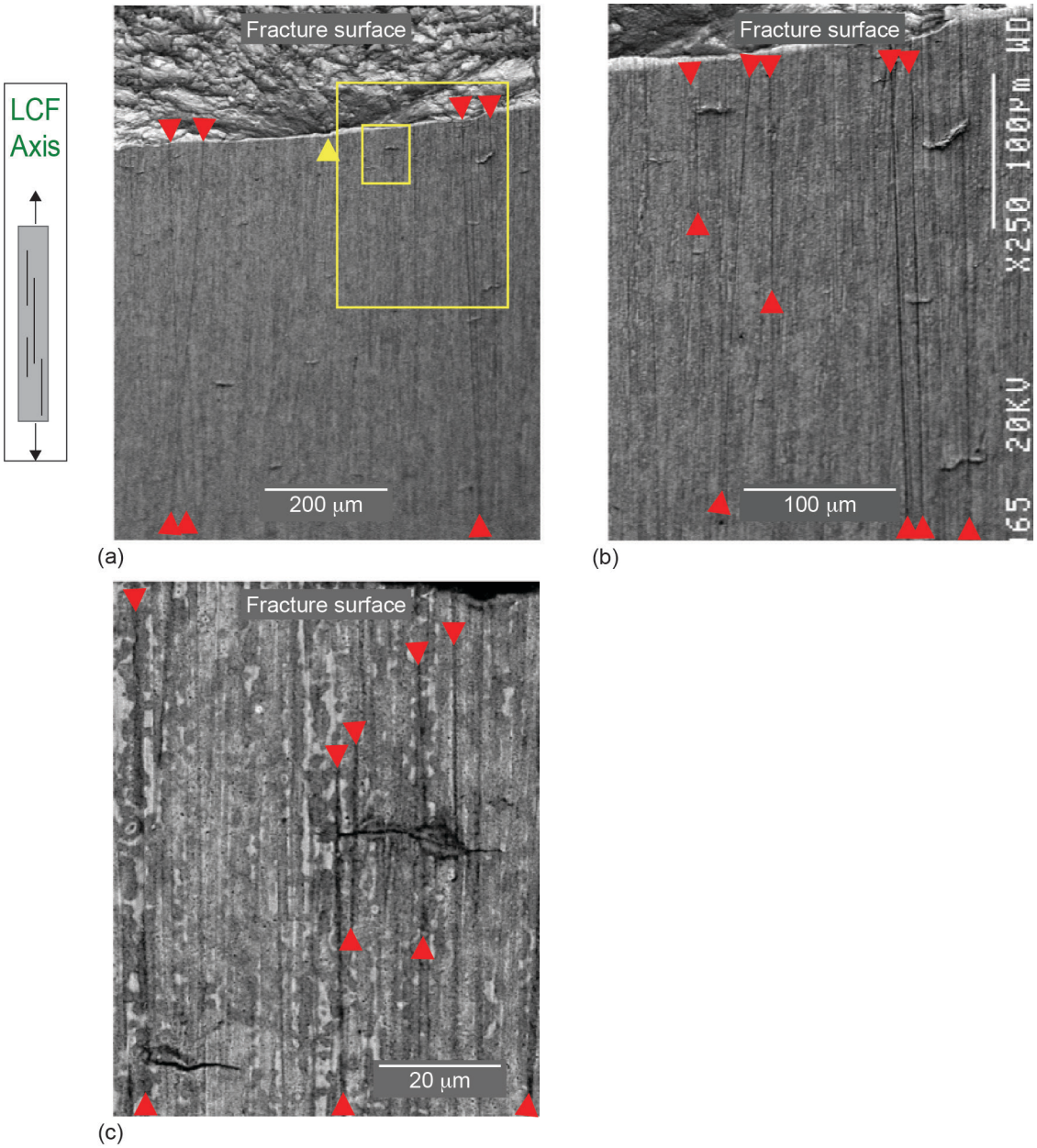

Figure 22.—BSE images (a) of the side of one the uncoated specimens showing the site of the primary crack initiation (yellow marker). The most obvious polishing marks are indicated by red arrowheads. (b,c) Magnified images of the highlighted boxes in (a).

Polished Cross-Sections

Sections were cut from one of the tested specimens for each of the six coating compositions as well as for one of the specimens in the uncoated condition. Three cuts of each specimen were made to allow views of the coating, or near-surface region in the case of the uncoated specimen, both perpendicular and parallel to the loading axis, as shown in Figure 23. The perpendicular cuts allow viewing the linear gaps parallel to the loading axis, and the parallel cuts allow views of the fatigue cracks, which lie perpendicular to the loading axis. The parallel cut was made to view the area where the primary crack originated, as indicated in Figure 23(a) (left). For the parallel mounted face shown in Figure 23(b), it was usually easy to identify the side where the crack initiated from the fracture morphology. In addition, the fatigue cracks on the side where the crack initiated were almost always narrower than the cracks where the specimen eventually failed, as shown in Figure 23(b) (right). This is due to the initial crack relieving stress on the side where the crack initiated, whereas the last portion of the sample to fail underwent significantly higher strains prior to failure. The one exception to the different crack widths on the two sides of the specimen was for the ***High Cr***, ***Thin*** specimen where the cracks were very wide on both sides, as will be shown below.

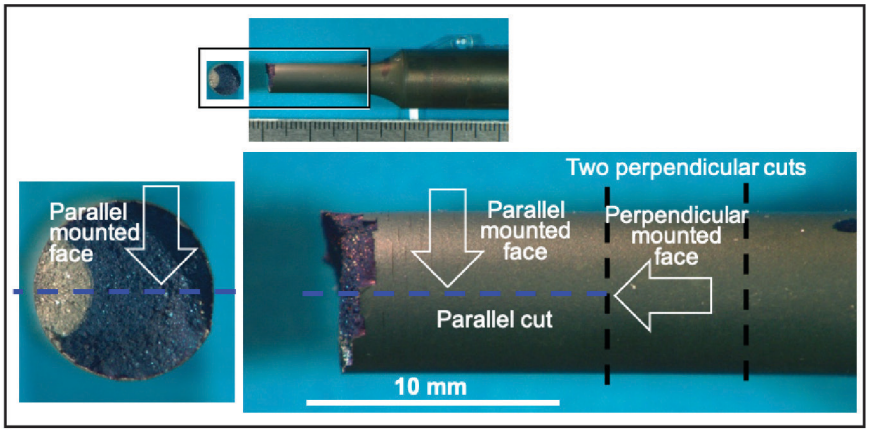

(a)

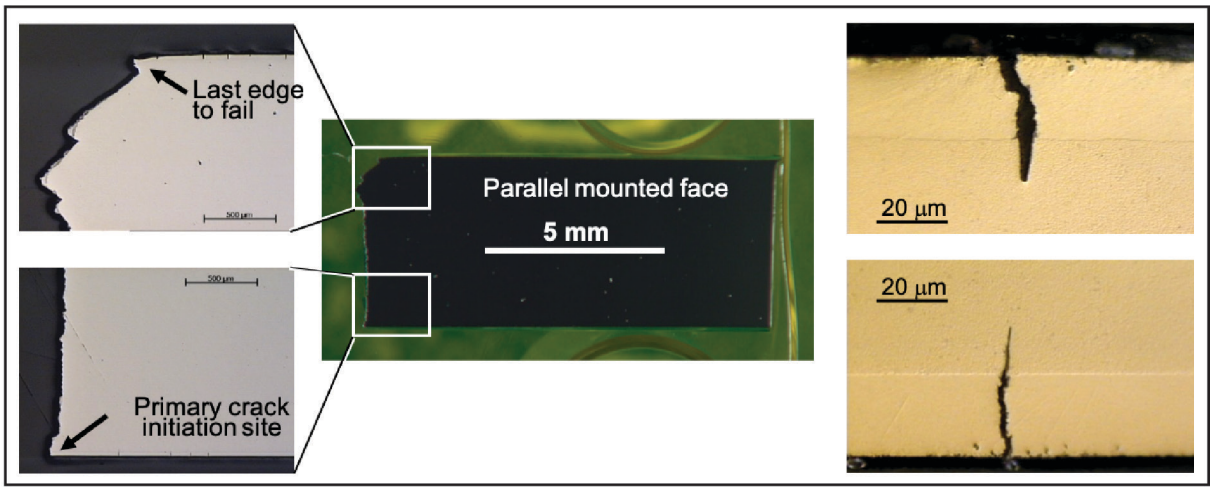

(b)

Figure 23.—(a) Macrophotos showing the orientation and position of the three cuts made on one half of the fractured LCF specimen. Two cuts perpendicular to the loading axis were made and one cut parallel to the loading axis. (b) optical images of the parallel mounted section showing the site of primary crack initiation (lower left) and representative cracks from the two sides of the specimen (upper and lower right).

Images for the ***Low Cr***, ***Thin*** coated specimen are shown in Figure 24. From the perpendicular views (a) to (d), (a) shows a cross-section of a typical spit, which penetrates nearly through the coating. Since it is unknown whether the spit was cut through the spit axis, it could have extended to the substrate. In (b), there is oxidation of an area representative of the shape of a spit. It could be that a loosely bonded spit was lost from this location and the exposed coating oxidized. The "crack" shown in (c) is one of the linear gaps running parallel to the rod axis which was present prior to LCF testing (see Figure 4). In (d), there is a large oxide formation in the substrate with scattered oxide particles in the coating. If the fatigue crack grows from the surface at an oblique angle to the rod axis, then the perpendicular cut can pass through the fatigue crack. If the crack was significantly oxidized, an image similar to that in Figure 24(d) could result. Hence, it is believed that the oxide in the substrate in Figure 24(d) is the result of the perpendicular cut, mount and polish plane passing through an oxidized fatigue crack. Images in Figure 24(e) to (h) are views taken along the parallel cut (Figure 23(a) and (b)) showing fatigue cracks passing through the coating and penetrating into the substrate. Extensive oxidation is present in the cracks, especially in the substrate. Since these cracks form during LCF testing, the oxidation occurs only during that period of LCF testing at 760 °C in air. It is apparent that oxidation has occurred at the crack tip. It should be noted that there was generally little oxidation in the coating due to the protective Cr_2O_3 formation. However, when oxygen penetrated down a crack into the substrate, significant oxidation of the substrate alloy was observed, typically filling the crack. Figure 24 also highlights the difference between the linear gaps (Figure 24(c)) and the fatigue cracks (Figure 24(e) and (g)). Since the linear gaps form during coating formation, oriented along the axis, they do not propagate during fatigue testing but remain only in the coating. Cr_2O_3, and likely some $NiCr_2O_4$ form on the walls of the gap, based on EDS indications.

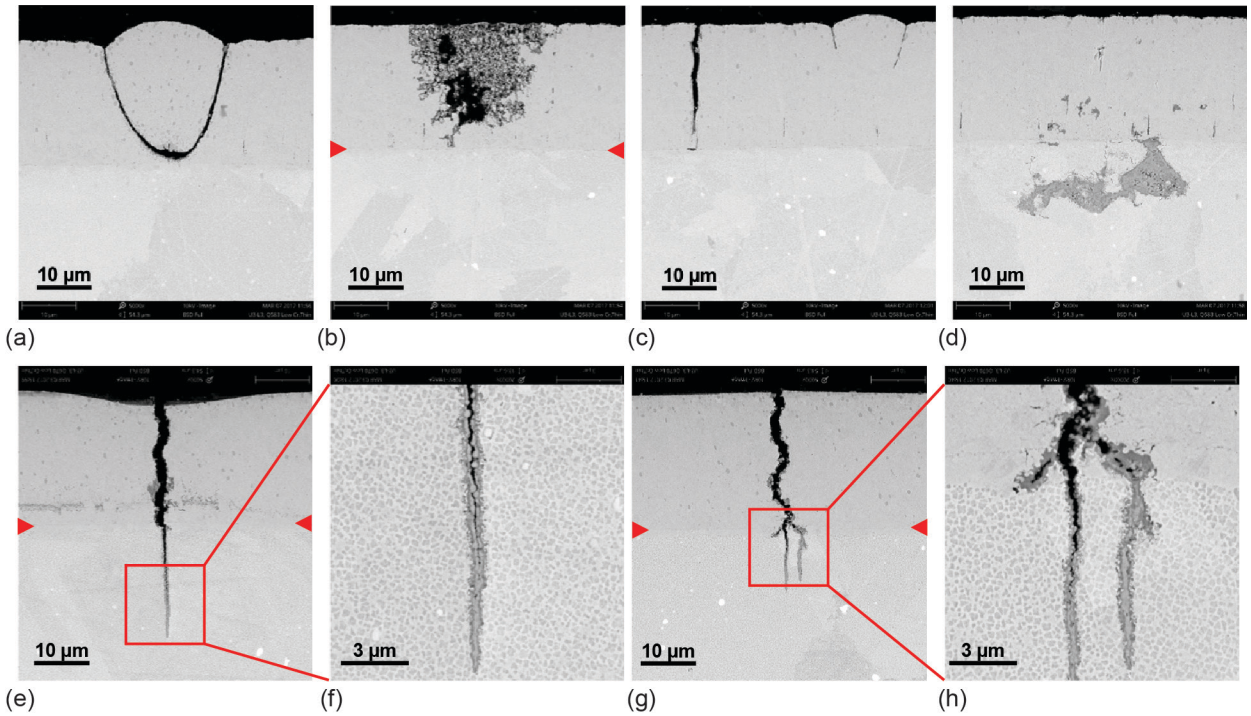

Figure 24.—BSE images of the ***Low Cr***, ***Thin*** coating after LCF testing showing (a-d) typical defects in the mount perpendicular to the loading axis, (a) spit penetrating most of the coating, (b) oxidized region (loss of a spit?), (c) linear gap defect parallel to the loading axis, and (d) large oxide formation in the substrate with some oxide particles in the coating. (e-h) BSE images from the mount parallel to the loading axis showing two fatigue cracks (e.g.,) (perpendicular to the loading axis) penetrating through the coating and into the substrate. (f,h) show that the crack tip in the substrate is oxidized.

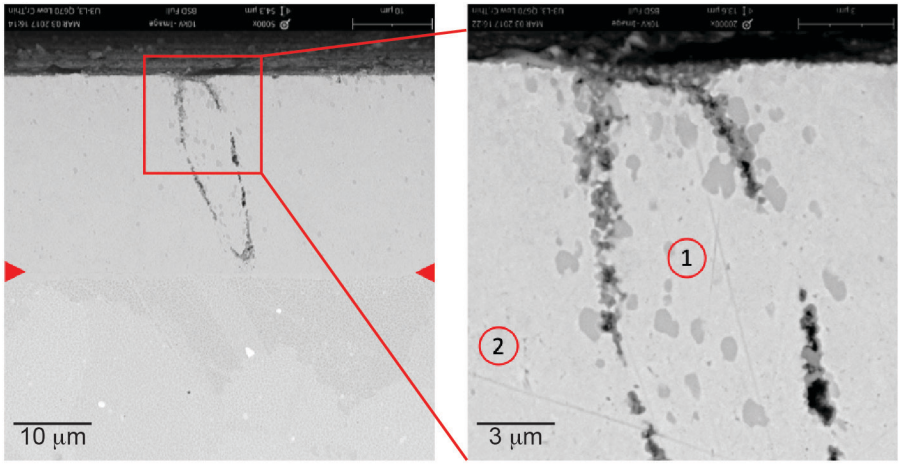

(a) (b)

	1	2
Ni (wt%)	72.28	71.94
Cr (wt%)	27.72	28.06

Figure 25.—BSE images of the ***Low Cr***, ***Thin*** coating after LCF testing showing (a,b) a spit in the coating. The second phase high in Cr is evident in the magnified view in (b). EDS measurements (Table) show that the composition of the matrix phase in the spit is the same as that of the surrounding coating.

However, fatigue cracks, being oriented perpendicular to the loading axis, propagate through the coating and into the substrate, as shown in Figure 24(e) and (g). Figure 25 shows the cross-section of a polished spit also in the ***Low Cr***, ***Thin*** coated specimen. The darker, high-Cr α phase is evident in the spit (Figure 25(b)). Surprisingly, EDS measurements of the FCC matrix phase in the spit and outside the spit show similar compositions. The Ni-Cr phase diagram shown previously (Figure 7(d)) indicates an equilibrium Cr concentration in the two-phase region of 34 wt%. It seems possible that the ejected spit was high in Cr resulting in the presence of the α-Cr particles, but the Cr concentration both inside and outside the spit (~28 wt%) appears lower than expected from the phase diagram but close to the measured Cr composition of the ***Low Cr*** coating (Table 2).

Each of the images shown in Figure 26 for the ***Med Cr***, ***Thin*** coated specimen are views from the parallel mounted face and show areas of oxidation around spits (a,b,d) and fatigue cracks of various lengths. The fatigue cracks appear to follow a more tortuous path in the coating than for the ***Low Cr***, ***Thin*** coating shown previously. Again, oxidation at the crack tip is evident. Images of the ***High Cr***, ***Thin*** coating from the perpendicular mount are shown in Figure 27. Oxidation around and below the spit in Figure 27(a) is likely the polishing plane passing through one of the wide fatigue cracks previously shown for this coating (Figure 18). An oxidized linear gap is shown in Figure 27(b) and (c). The large crack openings and high frequency of fatigue cracks observed on the surface of the specimen after LCF testing are apparent in the images of the parallel mounted face (Figure 28). Many of the wide cracks have penetrated into the substrate and are oxidized Figure 28(b) to (d). Given the width of the cracks penetrating into the substrate, it is somewhat surprising that this coating (***High Cr***, ***Thin***) showed the longest LCF life with 2 to 3 times the number of cycles than for the other coated specimens.

Images from the perpendicular cut of the ***Low Cr***, ***Thick*** coating are shown in Figure 29(a) to (c). Oxidation of one of the linear gaps is shown in Figure 29(a) and (b). What appears to be a deep trough in the coating, likely caused by the loss of a spit, is shown in Figure 29(c). In views along the parallel face, typical fatigue cracks are shown in Figure 29(d) to (g). It was not clear whether these cracks exhibited any more or less a tortuous path than those shown previously. The large linear gap defects parallel to the loading axis in the ***Med Cr***, ***Thick*** coating are seen in the views of the perpendicular mount in Figure 30(a) to (c). The poor bond between the coating and substrate is evident by the gap between the

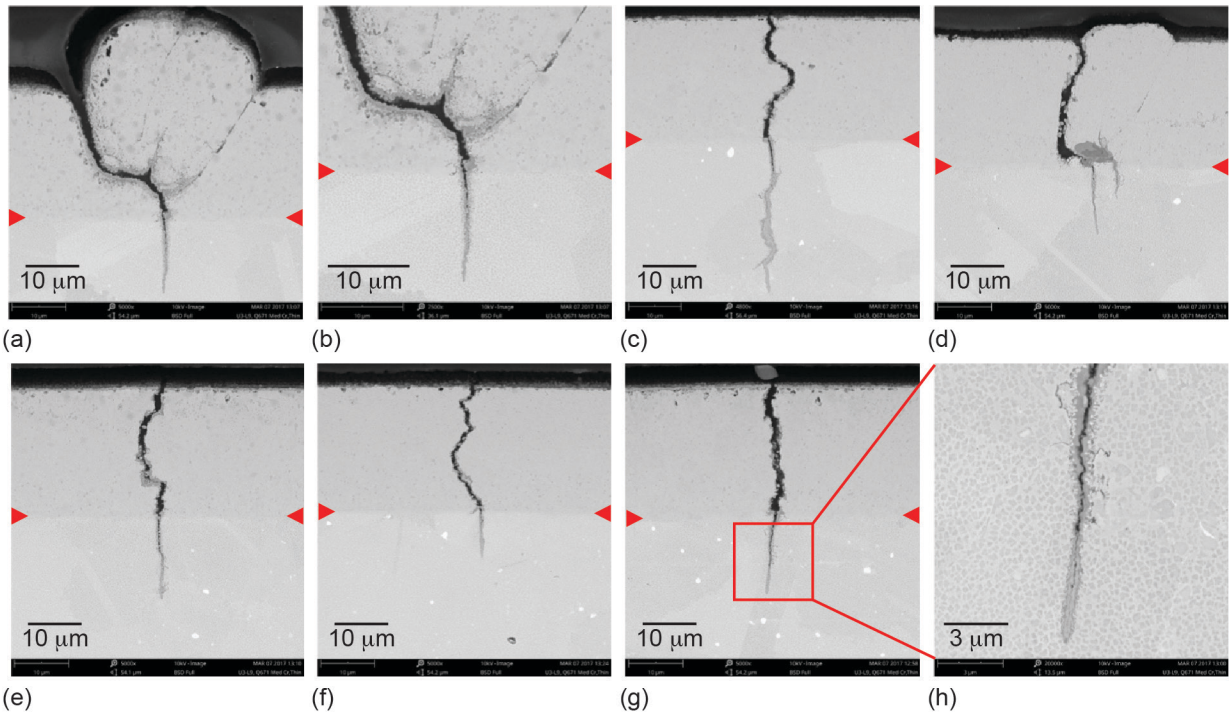

Figure 26.—BSE images taken along the parallel face of the ***Med Cr***, ***Thin*** coating after LCF testing showing (a,b) oxidation around a spit and down a crack penetrating into the substrate, (c-h) perpendicular fatigue cracks penetrating through the coating and into the substrate. Oxidation of the crack in the substrate is obvious.

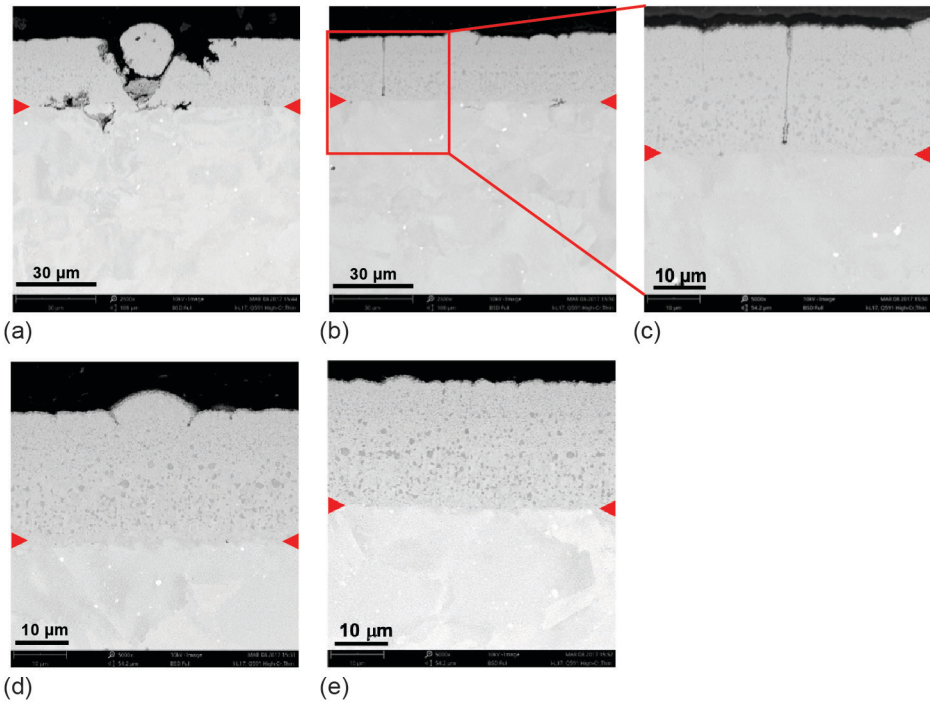

Figure 27.—BSE images of the ***High Cr***, ***Thin*** coating after LCF testing (perpendicular mount) showing (a) spit with oxidation (b) linear gap defect (c) higher magnification of the linear gap defect in (b), (d) spit defect, and (e) higher magnification image of the coating showing the α-Cr particles. The red arrowheads indicate the coating/substrate interface.

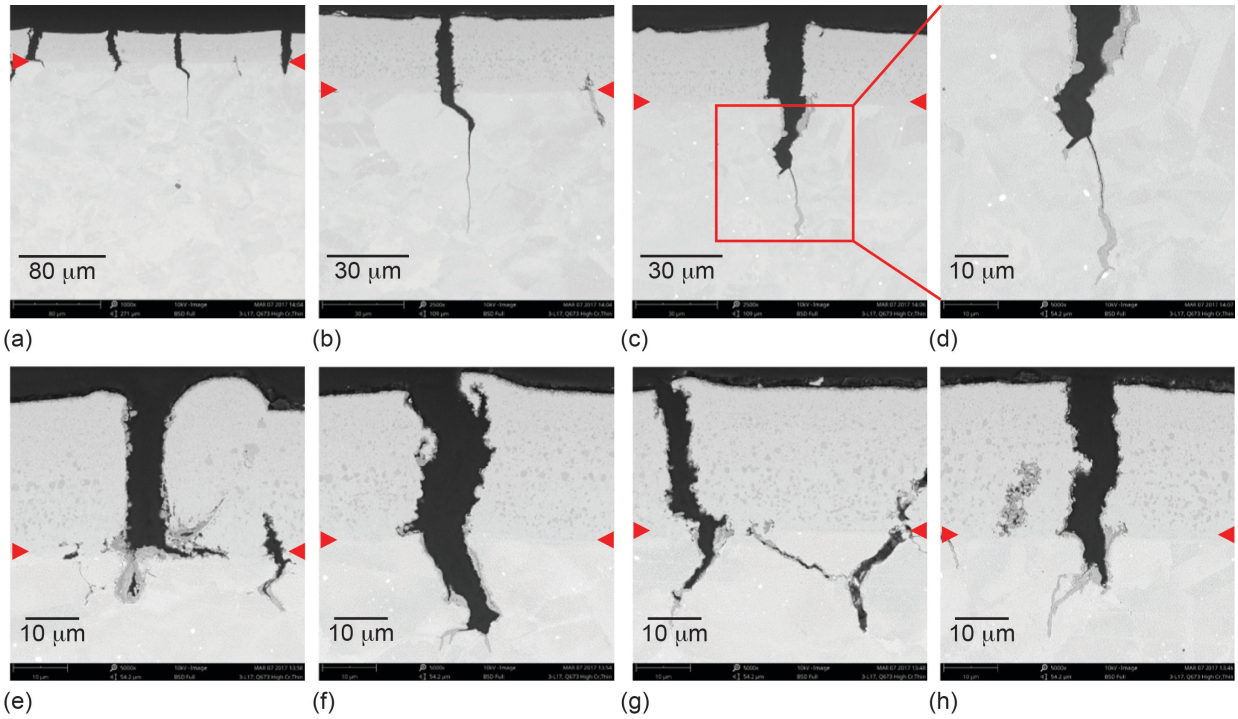

Figure 28.—BSE images of the ***High Cr***, ***Thin*** coating after LCF testing taken in the direction parallel to the loading axis showing (a) the close spacing of the fatigue cracks. (b-h) Various views of the fatigue cracks showing the wide gap. Oxidation of the cracks in the substrate is evident. The red arrowheads indicate the coating/substrate interface.

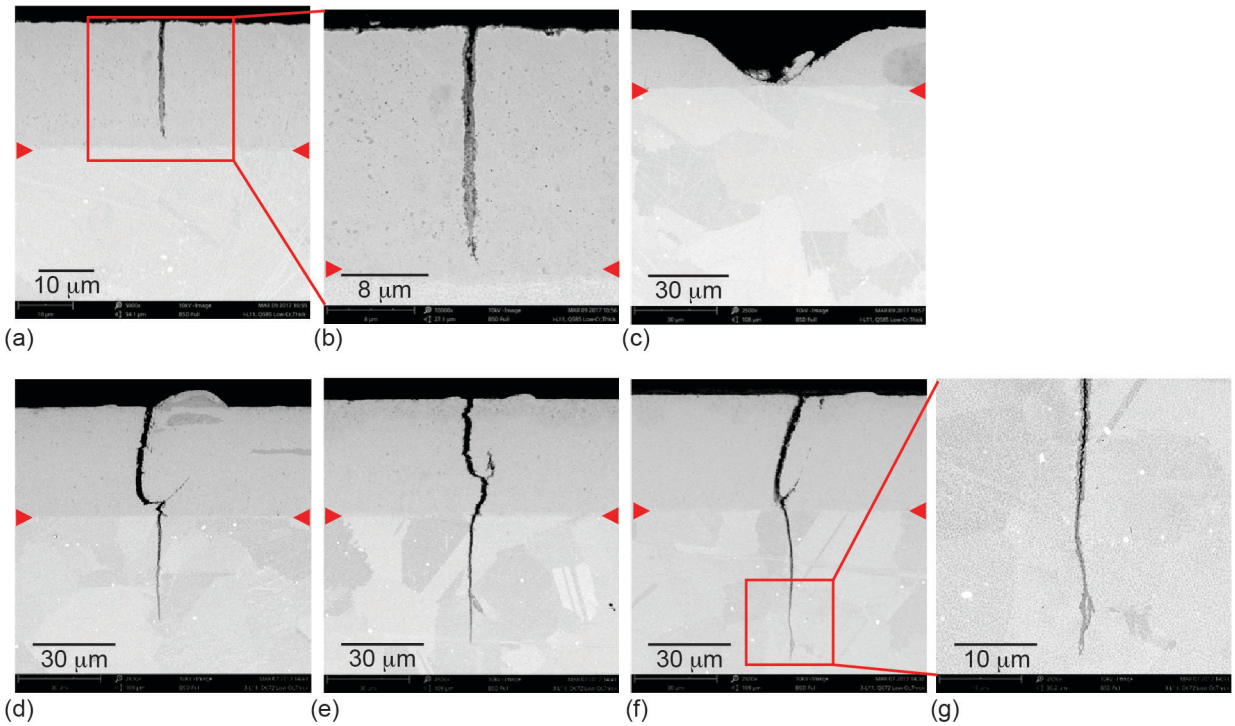

Figure 29.—BSE images of the ***Low Cr***, ***Thick*** coating after LCF testing showing (a,b) a linear gap defect in the coating filled with oxidation (perpendicular mount), (c-g) perpendicular fatigue cracks penetrating into the substrate (parallel mount).

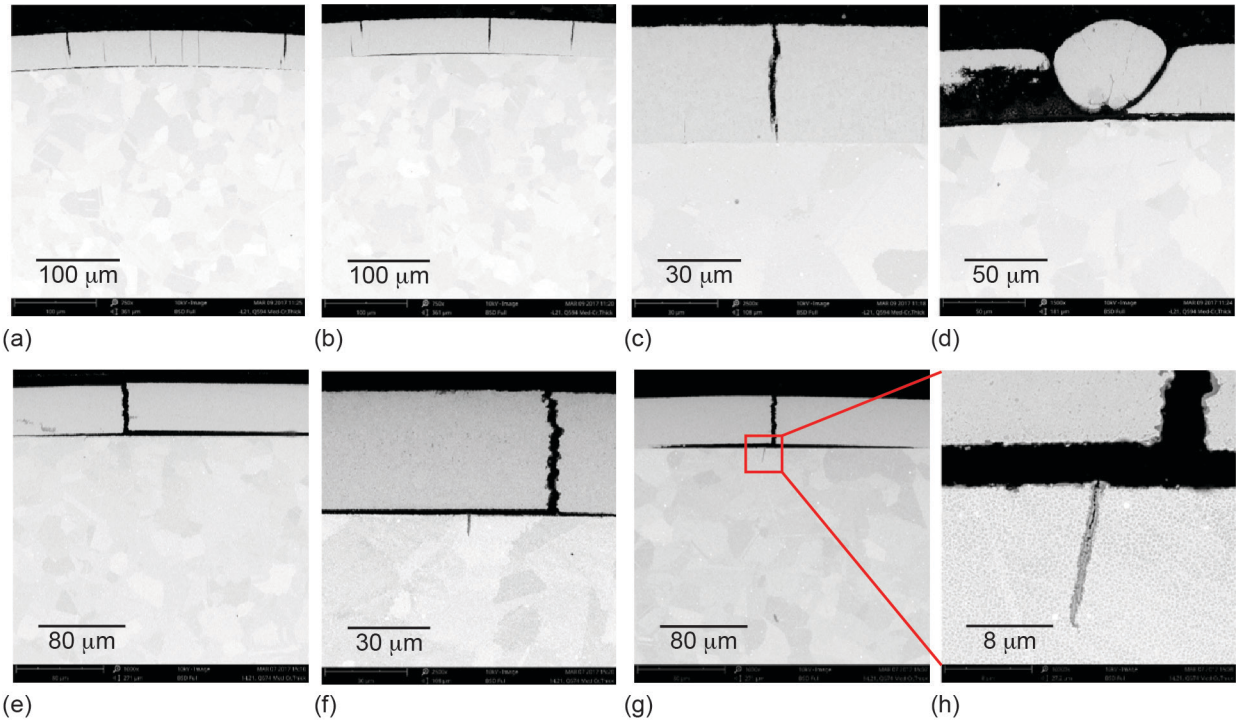

Figure 30.—BSE images of the ***Med Cr***, ***Thick*** coating after LCF testing (a, b) showing a poor bond of the coating to the substrate, (c) linear gap defects parallel with the loading axis, (d) a large spit in the perpendicular mount. (e-h) Images from the parallel mount showing fatigue cracks oriented perpendicular to the loading axis. Debonding of the coating is also evident.

coating and substrate. A linear gap and spit are clearly seen in Figure 30(c) and (d). In views along the parallel mount Figure 30(e) to (h), fatigue cracks are evident but it appears some of the cracks have been blunted by the poor bond of the coating. Some smaller fatigue cracks, not aligned with the cracks in the coating, can be seen penetrating into the substrate. Lastly, similar defects to those previously observed were also apparent in the polished sections of the ***Med Cr+ZrO_2***, ***Thin*** coating. Figure 31(a) shows a linear gap with the outer ZrO_2 layer, Figure 31(b) and (c) shows a spit and a highly oxidized region which appears associated with a spit. Oxidized fatigue cracks, similar to those shown above, are evident in the parallel views in Figure 31(d) to (f). There were several crack-like defects that appear totally within the coating, as shown in Figure 31(g). Most of these defects appeared to be highly angled with respect to the surface.

Representative images of the uncoated specimens after LCF testing are shown in Figure 32. In the views of the perpendicular cut Figure 32(a) to (d), small oxide-filled cracks or defects are obvious. The origin of these features is not clear since the depths of the polishing marks are much less than the depths of these defects. They may be the result of the polishing plane passing through a fatigue crack, or they may be related to oxidation of a substrate feature (e.g., carbide). In the views parallel to the specimen axis (Figure 32(e) to (h)), very small fatigue cracks, approximately 10 µm deep, are apparent. As indicated earlier by the views of the specimen surface (Figure 19, Figure 20, and Figure 22), perpendicular fatigue cracks on the uncoated specimens were much less frequent than for the coated specimens.

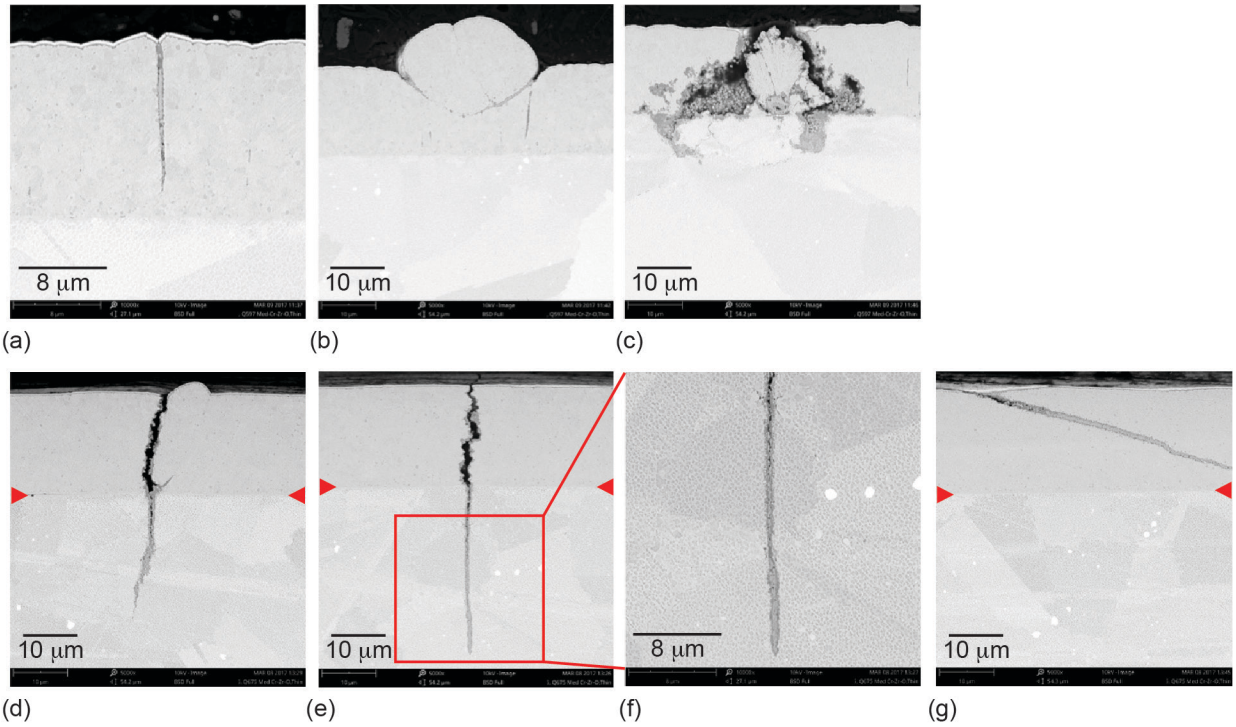

Figure 31.—BSE images of the ***Med Cr_Zr-O***, ***Thin*** coating after LCF testing showing (a-c) oxidized linear gap defect, spit and an oxidized defect with oxide penetration into the substrate (perpendicular mount). (d-f) Typical perpendicular fatigue cracks and (g) a linear defect in the coating seen in the parallel mounts.

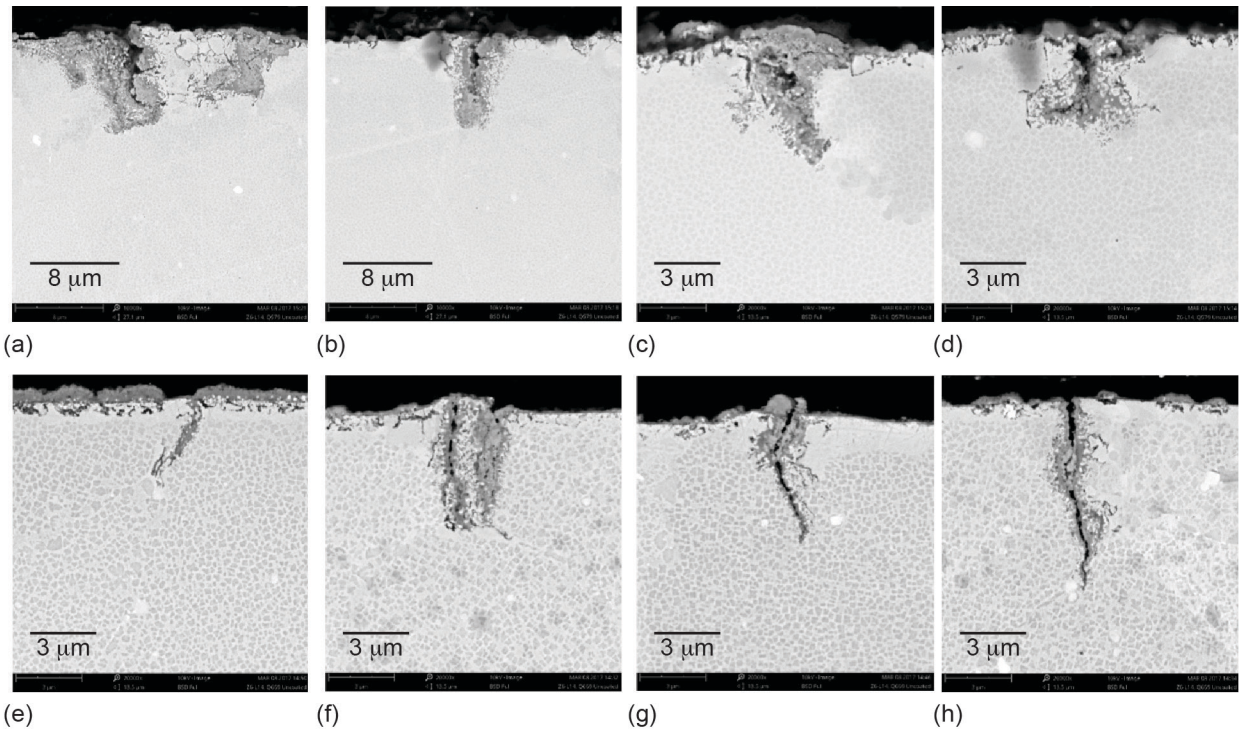

Figure 32.—BSE images of one of the uncoated LCF specimens after LCF testing, (a-d) perpendicular cut showing oxide filled axial cracks, and (e-h) parallel cut showing oxide filled fatigue cracks running perpendicular to the loading axis.

Discussion

The design philosophy followed in this study was to examine coatings that were relatively thin and ductile. It was believed that a thin, ductile coating would easily deform with any strains in the substrate and minimize any effect on the LCF life. Ni-Cr coatings were selected both for ductility and as Cr_2O_3 formers for oxidation and corrosion protection. However, it is clear that the presence of the coating alone, without any significant environmental exposures, degraded the LCF life of the disk alloy. In addition, it was surprising that the LCF life increased with Cr content, contrary to what was anticipated based on the expected ductility of the coatings. As stated earlier, this debit due to the presence of a coating has been observed in other fatigue studies. T.N. Rhys-Jones, in an early overview, referred to this coating debit as a "fatigue strength and life penalty," stating that this penalty with the coating was acceptable in comparison to the very significant degradation, which occurs during environmental exposures without the coating (Ref. 61). Hence, the real value of these coatings cannot be assessed until after observing the effect of oxidation and hot corrosion on the coated and uncoated samples, which has been delayed until Part II. However, there are several interesting observations to discuss, including the high incidence of cracking in the coatings, the observation that most of the cracks were arrested at the coating/substrate interface, and the observation of more cracking in the ***High Cr***, ***Thin*** coating yet which showed the highest LCF life.

It might appear that the debit in the LCF life in the current study is due to the multitude of cracks initiating at the surface and propagating through the coating resulting in a "premature" failure in comparison to the uncoated case. However, although several other studies have reported an increased number of secondary cracks in the coatings (Refs. 26, 63, 67, and 68), some of those studies have also reported an increase in the LCF life in spite of the additional cracks (Refs. 26, 63, and 67). Wood, in an early study with MCrAlY coatings, observed significant secondary cracking in the coating at high temperature (800 °C) yet without a detrimental effect on the LCF life, whereas testing at room temperature resulted in significantly less cracking in the coating, but a lower LCF life in comparison to the uncoated case (Ref. 79). Hence, the effect of increased cracking in the coating is uncertain and does not always result in early failures.

Comparing the mechanical properties and structure of the current NiCr-Y coatings with that of the substrate helps explain the increased cracking in the coatings. The coatings, without specific strengthening elements or grain boundary strengtheners, are obviously much weaker than the disk alloy which is optimized for mechanical strength (Ref. 19), includes carbides as grain boundary strengtheners, and is processed to produce fine grains, all of which help resist crack initiation and propagation. In addition, recent room temperature residual stress measurements showed that as-machined LCF specimens of the LSHR disk alloy possessed compressive stresses at the surface which remained after thermal exposures at 760 °C (Refs. 19 and 27). In contrast, room temperature residual stress measurements of the as-deposited, High-Cr coating revealed a tensile stress at the surface of the coating (Refs. 19 and 27). However, following shot peening, which compressively loaded the coating, the coating relaxed after thermal exposures at 760 °C with a tensile surface stress again at room temperature. In contrast, the substrate, after identical shot peening and thermal exposures, retained some of the compressive loading emphasizing the significant difference in the mechanical strength of the coating in comparison to the substrate. The total relaxation of the coating after exposures at 760 °C suggests the coating is relatively stress-free when undergoing LCF testing at 760 °C whereas the substrate likely remains under compressive stress. Hence, due to the strength, morphology and compressive loading of the substrate, it is not surprising that most of the cracks in the coating arrest at the coating/substrate interface.

The cause of the tensile stress in the coating when cooled to room temperature is likely due to the CTE mismatch between the coating and substrate. Recent measurements have shown that high-Cr NiCr alloys have a higher CTE than that of the disk alloy (Ref. 19). Since the coatings are likely stress free at 760 °C, cooling to room temperature results in a tensile stress in the thin coatings. It should also be noted that the CTE mismatch and tensile stress in the coating at room temperature does not appear to be sufficient to cause cracking since thermal cycling of ME3 pins coated with the ***High Cr*** coating underwent 1020 1-hr cycles at 760 °C in air without any cracking of the coating (Ref. 16). Hence, stress associated with LCF cycling is necessary to produce the cracks observed in the coating.

Returning to the causes of increased cracking in the coating, the morphology of the coating itself could promote this increased cracking. PVD coatings, when deposited at intermediate homologous temperatures ($T_{deposition,K}$ ~0.4-0.8$T_{melt,K}$), as in the present study, often have a columnar microstructure (Ref. 76). This columnar structure is indicated by the vertical gaps shown in the polished microstructures (Figure 6). Obviously, this columnar structure allows easier crack propagation through the coating along the columnar grain boundaries and along the columnar gaps. Although it is possible to deposit a PVD coating at very high homologous temperatures ($T_{dep} \geq 0.9T_{m,K}$) resulting in recrystallization with finer, equiaxed grains, those deposition temperatures could result in significant interdiffusion during coating deposition as well as coarsening of the fine grain structure of the disk alloy (Ref. 57). Hence, the coating morphology produced by the PVD process likely enhances crack propagation through the coating.

Lastly with respect to increased cracking of the coating is the presence of the spit defects on the surface. These defects, attributable to the coating process and dispersed across the surface, provide preferred sites for crack initiation. There was significant evidence that the spits were weakly bonded to the surrounding coating, such as oxidation at the interface of the spits, “holes” in the coating indicating the loss of a spit and the observation that many of the longitudinal cracks/defects passed around the spits. In addition, most of the fatigue cracks shown on the surface in Figure 14, Figure 15, Figure 17, and Figure 18 are associated with a spit. During the post-test failure analysis of the fracture surfaces, spits were often observed at the primary crack initiation site. Hence, it seems clear that the poorly bonded spits on the surface act as initiation sites for fatigue cracking. Therefore, given the fact that the coatings are relatively weak in comparison to the substrate, are stress-free at the test temperature, possess a columnar morphology and contain spits, it is not surprising that the coatings exhibit significantly more cracks than the uncoated disk alloy specimens. Although it is apparent that the spits need to be eliminated from the coating, different techniques to eliminate the spits have been proposed by the coating vendor but have not been totally successful to date. It is likely that some different processing procedures will reduce the number and impact of these defects.

It is not surprising that most of the cracks were arrested at the coating/substrate interface, given the differences in strength, residual stress, and morphology/microstructure between the coating and substrate stated above. Whereas the coating cracks easily due to the spits, columnar morphology, and stress-free condition, the substrate is designed to resist cracking with a fine grain microstructure, grain boundary strengtheners and with the additional benefit of a residual compressive stress remaining from processing. As indicated above, there have been many studies which report a large number of secondary cracks in coatings (Refs. 26, 63, 67, and 68), and where stated, most of those cracks were arrested at the coating/ substrate interface (Refs. 63 and 68).

In contrast to the increased cracking in the coating and crack arresting at the substrate, it was surprising that the most cracking was observed in the ***High Cr***, ***Thin*** coating and that this coating showed the highest LCF life. Furthermore, the ***High Cr*** coating would be expected to have the lowest ductility of the three coating compositions. As stated repeatedly above, NiCr-Y coatings were selected in the present study for their oxidation and hot corrosion protection as well as their high ductility. Whereas the strength

of a Ni-Cr coating would be expected to increase with Cr content, the ductility, typically being inversely related to strength, would therefore be expected to decrease with Cr content. Hence, it would be expected that the ductility would be highest for the ***Low Cr*** coating and lowest for the ***High Cr*** coating. Conversely, since the matrix of the ***High Cr*** coating is saturated with Cr and contains a higher volume fraction of the α phase, it is likely that this coating is mechanically the strongest of the three coating compositions. Hence, the results of this study were contrary to expectations since the coating with the highest ductility (***Low Cr***, ***Thin***) exhibited the lowest LCF life and the coating with the highest strength and lowest ductility (***High Cr***, ***Thin***), exhibited the highest LCF life. Consequently, the LCF life of a coated disk alloy does not appear to scale with coating ductility but with coating strength, or perhaps coating strength is a stronger factor than ductility affecting LCF life.

It is also surprising that the coating with the highest LCF life also showed the most surface cracking. Moreover, the amount of surface cracking appears to scale directly with the Cr content (and presumably strength), as can be seen qualitatively by comparing Figure 14(c) (***Low Cr***, ***Thin***), Figure 15(c) (***Med Cr***, ***Thin***), and Figure 18(d) (***High Cr***, ***Thin***), all shown at the same magnification. Hence, the variation in the amount of cracking in the coating could, at least in part, be related to the coating ductility or coating strength linked to the coating composition. However, other factors could be controlling the amount of cracking in the coatings. A closer examination of the surfaces in the above referenced figures shows that the number of spits on the surface of the coating is also highest in the ***High Cr***, ***Thin*** coating. In the ***Med Cr*** and ***High Cr*** coatings, the higher Cr concentrations were produced by increasing the power of the second target of pure Cr. It is possible that additional spits were produced as the power was increased to this second target. As stated previously, the poorly bonded spits present sites for easier crack initiation, which explains why nearly every fatigue crack in the preceding figures is associated with a spit. Hence, the fabrication process resulting in increasing spits with increasing Cr content could contribute to the observed increase in the surface cracking in the ***Med Cr*** and ***High Cr*** coatings.

The role of oxidation in the fatigue cracks is uncertain but likely increases the crack propagation rate. Oxidation of the cracks in the coating was generally much less than the oxidation, which occurred when the cracks penetrated the substrate. This is expected since a thin, protective layer of Cr_2O_3 was likely formed in the NiCr-Y coating whereas Cr_2O_3, Al_2O_3 and TiO_2 (Ref. 33), likely formed in the substrate. However, there were some significant regions of oxidation in the coating primarily associated with spits (Figure 24(b), Figure 26(a), (b), Figure 27(a), Figure 28(e), and Figure 31(c)). There was also more oxide in the linear gaps in the coating, which formed along the longitudinal polishing marks (Figure 29(a), (b), and Figure 31(a)). The increased oxidation in these gaps is reasonable since these linear gaps existed following coating formation and underwent the 8 hr low PO_2 diffusion anneal as well as being oxidized at the start of fatigue testing whereas the fatigue cracks do not oxidize until the cracks initiated and propagated. In one recent study with the ***High Cr*** coating, which had been shot peened, fatigue cracks were not observed until half of the fatigue life of the specimen (Ref. 19). Hence, the linear gaps could have more than twice the exposure time as a fatigue crack. Note that since oxidation of the cracks only occurred after crack initiation during the fatigue testing, specimens which experienced a longer fatigue life also experienced a longer oxidation exposure, as indicated in the "LCF Test Time (hr)" column in Table 3.

The cracks which penetrated the disk alloy appeared to penetrate into the substrate in a largely transgranular manner (Figure 24, Figure 26, Figure 29, and Figure 31) although some cracking started intergranular over the first grain boundary (Figure 28). It is interesting to note that there appears to be no γ' depletion surrounding the crack tip (Figure 24(f), (h), and Figure 26(h)). This is likely due to the rate of crack growth and the low temperatures reducing diffusional transport of the oxygen-active elements (Cr, Al, Ti) from the surrounding area from moving to the crack as was observed in other studies at higher

temperatures (Ref. 35). This is significant in that γ'-depleted zones are often credited with weakening the matrix locally and contributing to the crack growth (Refs. 14, 26, 29, 35, and 38) which does not appear to be relevant in the present case. It is well known that oxidation reduces the fatigue life of Ni-base alloys and it is generally proposed that oxidation occurs ahead of the crack tip via oxygen diffusion within the grain boundaries or by a stress-enhanced mechanism (Refs. 39, 41, and 42).

The longitudinal polishing marks in the substrate that resulted in the formation of the linear gaps in the coating are considered of secondary importance. In the present study, the linear gaps, aligned along the loading axis, were observed at the primary crack initiation site indicating a possible role in primary crack initiation. In addition, many of these linear gap defects extended through the coating allowing oxygen to easily reach the substrate. However, recent research with various pre-coat surface treatments has resulted in a coating morphology without these undesirable features (Ref. 80). Without a coating, the polishing marks appear to be inconsequential in fatigue testing. Hence, current studies with PVD NiCr-Y coatings show no indications of the linear gaps.

It is unknown why the coating/substrate interface was so weak for the ***Med Cr***, ***Thick*** coating. After the Low PO_2 diffusion anneal, the coating showed regions of debonding with many of the linear gaps extending through the coating to the substrate. Hence, issues with bonding were present before the LCF testing. After LCF testing, the lack of bonding was more apparent with gaps between the coating and substrate (Figure 16). The primary crack initiated in an area where the coating was bonded to the substrate (Figure 16(b)), which shows the potentially deleterious effect of the coating where early cracking can penetrate into the substrate. In regions where the coating was only weakly bonded, or not bonded at all, any cracks that propagated through the coating were arrested at the weak coating/substrate interface (Figure 30). Although it is well known that thicker coatings may possess greater stress after deposition, the ***Low Cr***, ***Thick*** coating, with a similar thickness, showed no coating/substrate bond weakness. It is possible that with a lower Cr content, this latter coating was mechanically weaker and able to deform and relieve stresses produced by the thick deposit. However, it is also possible that something occurred before, or early during the coating run affecting the specimen surfaces resulting in the poor coating/substrate bonding. It should be noted that there was no issue with bond adherence in the coating run following the ***Med Cr***, ***Thick*** coating run (***Med Cr+ZrO_2***, ***Thin***). Additional work would be needed to determine whether the weak bond was associated with that particular coating composition and thickness combination, or whether a different issue caused the lack of bonding.

It appears that the thickness of the coating, for the thicknesses examined, plays a small role. Since the cause of the bonding issue with the ***Med Cr***, ***Thick*** coating is unclear, only the ***Low Cr***, ***Thin*** and ***Low Cr***, ***Thick*** coatings can be compared indicating a slightly higher life with the thinner coating, although the increase is small. Lastly, the ***Med Cr+ZrO_2***, ***Thin*** coating showed a similar LCF life to the ***Med Cr***, ***Thin*** coating indicating the thin ZrO_2 layer on the surface had a negligible effect on the LCF life. As stated above, the value of the thin ZrO_2 layer will have to be evaluated after oxidation and hot corrosion exposures.

Conclusions

1. Application of NiCr-Y coatings by PEMS reduced the LCF life of the disk alloys.
2. The LCF life increased with increasing Cr content of the coating.
3. There was significantly more secondary cracking in the coating than in the uncoated substrate, with the amount of this secondary cracking increasing with Cr content of the coating.
4. Most of the secondary cracks were arrested at the substrate.
5. Oxidation down cracks into the substrate likely enhanced crack growth.
6. Spits (aka “molten droplets”) ejected from the target and deposited on the surface act as crack initiation sites.

References

1. M. Dowd, K.M. Perkins, and D.J. Child, "Pre-notched and corroded low cycle fatigue behaviour of a nickel based alloy for disc rotor applications," International Journal of Fatigue, 105, 7–15 (2017).
2. A.K. Misra and L.A. Greenbauer-Seng, "Aerospace Propulsion and Power Materials and Structures Research at NASA Glenn Research Center," Journal of Aerospace Engineering, 26 (2), 459–490 (2013).
3. M.R. Bache, J.P. Jones, G.L. Drew, M.C. Hardy, and N. Fox, "Environment and time dependent effects on the fatigue response of an advanced nickel based superalloy," International Journal of Fatigue, 31 (11–12), 1719–1723 (2009).
4. A. Encinas-Oropesa, G.L. Drew, M.C. Hardy, A.J. Leggett, J.R. Nicholls, and N.J. Simms, "Effects of oxidation and hot corrosion in a nickel disc alloy," Superalloys 2008, The Mining, Metallurgy, and Materials Society, Warrendale, PA, 2008, pp. 609–618 (2008).
5. J.R. Nicholls, "Advances in Coating Design for High-Performance Gas Turbines," MRS Bulletin, 28 (09), 659–670 (2003).
6. R. Darolia, "Development of strong, oxidation and corrosion resistant nickel-based superalloys: critical review of challenges, progress and prospects," International Materials Reviews, DOI: 10.1080/09506608.2018.1516713, pp. 26 (2018).
7. G.W. Goward, "Protective coatings – purpose, role, and design," Materials Science and Technology, 2 (3), 194–200 (1986).
8. G.W. Goward, "Progress in coatings for gas turbine airfoils," Surface and Coatings Technology, 108, 73–79 (1998).
9. A. Pineau and S.D. Antolovich, "High temperature fatigue of nickel-base superalloys – A review with special emphasis on deformation modes and oxidation," Engineering Failure Analysis, 16 (8), 2668–2697 (2009).
10. R. Schafrik and R. Sprague, "Superalloy Technology - A Perspective on Critical Innovations for Turbine Engines," Key Engineering Materials, 380, 113–134 (2008).
11. A.K. Misra, "Durability challenges for next generation of gas turbine engine materials," in *AVT Symposium on Design, Modelling, Lifting and Validation of Advanced Materials in Extreme Military Environments*; (AVT, Biarritz; France, 2012).
12. D. Furrer and H. Fecht, "Ni-based superalloys for turbine discs," JOM, 51 (1), 14–17 (1999).
13. G.J. Gibson, K.M. Perkins, S. Gray, and A.J. Leggett, "Influence of shot peening on high-temperature corrosion and corrosion-fatigue of nickel based superalloy 720Li," Materials at High Temperatures, 33 (3), 225–233 (2016).
14. S. Li, X. Yang, G. Xu, H. Qi, and D. Shi, "Influence of the different salt deposits on the fatigue behavior of a directionally solidified nickel-based superalloy," International Journal of Fatigue, 84, 91–96 (2016).
15. T.P. Gabb, J. Telesman, B. Hazel, and D.P. Mourer, "The Effects of Hot Corrosion Pits on the Fatigue Resistance of a Disk Superalloy," Journal of Materials Engineering and Performance, 19 (1), 77–89 (2009).
16. T.P. Gabb, R.A. Miller, C.K. Sudbrack, S.L. Draper, J.A. Nesbitt, R.B. Rogers, J. Telesman, Ngo, and J. Healy, "Cyclic Oxidation and Hot Corrosion of NiCrY-Coated Disk Superalloys," NASA/TM—2016-219105, Washington, D.C., June 2016.
17. J.R. Nicholls, "Designing oxidation-resistant coatings," JOM, 52 (1), 28–35 (2000).
18. N. Eliaz, G. Shemesh, and R.M. Latanision, "Hot corrosion in gas turbine components," Engineering Failure Analysis, 9 (1), 31–43 (2002).

19. T.P. Gabb, R.B. Rogers, J.A. Nesbitt, R.A. Miller, B.J. Puleo, D. Johnson, J. Telesman, S.L. Draper, and I.E. Locci, "Influences of Processing and Fatigue Cycling on Residual Stresses in a NiCrY-Coated Powder Metallurgy Disk Superalloy," Journal of Materials Engineering and Performance, 26 (11), 5237–5250 (2017).
20. T.J. Carter, "Common failures in gas turbine blades," Engineering Failure Analysis, 12 (2), 237–247 (2005).
21. J.C. Williams and E.A. Starke, "Progress in structural materials for aerospace systems," Acta Materialia, 51 (19), 5775–5799 (2003).
22. P. Kantzos, P. Bonacuse, J. Telesman, T.P. Gabb, R. Barrie, and A. Banik, "Effect Of Powder Cleanliness On The Fatigue Behavior Of Powder Metallurgy Ni-Disk Alloy Udimet 720," Superalloys 2004, The Minerals, Metals & Materials Society, Warrendale, PA, pp. 409–417 (2004).
23. D.R. Chang, D.D. Krueger, and R.A. Sprague, "Superalloy Powdier Processing, Properties And Turbine Disk Applications," Superalloys 1984, The Minerals, Metals & Materials Society, Warrendale, PA, pp. 245–273 (1984).
24. E.S. Huron and P.G. Roth, "The Influence of Inclusions on Low Cycle Fatigue Life in a P/M Nickel-Base Disk Superalloy," Superalloys 1996, The Minerals, Metals & Materials Society, Warrendale, PA, pp. 359–368 (1996).
25. R.L. Barrie, T.P. Gabb, J. Telesman, P.T. Kantzos, A. Prescenzi, T. Biles, and P.J. Bonacuse, "Effectiveness of Shot Peening in Suppressing Fatigue Cracking at Non-metallic Inclusions in Udimet® 720," Materials Science and Engineering: A 474 (1–2), 71–81 (2008).
26. S.-L. Li, H.-Y. Qi, and X.-G. Yang, "Oxidation-Induced Damage of an Uncoated and Coated Nickel-based Superalloy under Simulated Gas Environment," Rare Metals 37 (3), 204–209 (2018).
27. T.P. Gabb, R.A. Miller, J.A. Nesbitt, S.L. Draper, R.B. Rogers, and J. Telesman, "The Effectiveness of a NiCrY-Coating on a Powder Metallurgy Disk Superalloy," NASA/TM—2018-219885, Washington, D.C., April 2018.
28. M.R. Bache, J. O'Hanlon, D.J. Child, and M.C. Hardy, "High Temperature Fatigue Behaviour in an Advanced Nickel Based Superalloy: The Effects of Oxidation and Stress Relaxation at Notches," Theoretical and Applied Fracture Mechanics 84, 64–71 (2016).
29. T.P. Gabb, C.K. Sudbrack, S.L. Draper, R.A. MacKay, and J. Telesman, "Effects of Long Term Exposures on Fatigue of PM Disk Superalloys," Materials Performance and Characterization 3 (2), 1–24, (2014).
30. T.P. Gabb, C.K. Sudbrack, S.L. Draper, R.A. MacKay, and J. Telesman, "Effects of Long Term Exposures on PM Disk Superalloys," NASA/TM—2013-216614, Washington, D.C., December 2013.
31. C.K. Sudbrack, S.L. Draper, T.T. Gorman, J. Telesman, T.P. Gabb, and D.R. Hull, "Oxidation and the Effects of High Temperature Exposures on Notched Fatigue Life of an Advanced Powder Metallurgy Disk Superalloy," Superalloys 2012, ed. E.S. Huron, R.C. Reed, M.C. Hardy, M.J. Mills, R.E. Montero, P.D. Portella, J. Telesman, The Minerals, Metals & Materials Society, Warrendale, PA, 2012, pp. 863–872.
32. T.P. Gabb, J. Telesman, P.T. Kantzos, and A. Garg, "Effects of Temperature on Failure Modes for a Nickel-Base Disk Superalloy," Journal of Failure Analysis and Prevention 7 (1), 56–65 (2007).
33. S.D. Antolovich, P. Domas, and J.L. Strudel, "Low Cycle Fatigue of René 80 as Affected by Prior Exposure," Metallurgical Transactions A 10 (12), 1859–1868 (1979).
34. S. Bashir, P. Taupin, and S.D. Antolovich, "Low Cycle Fatigue of as-HIP and HIP+ Forged René 95," Metallurgical Transactions A 10 (10), 1481–1490 (1979).

35. A. Gordon, R. Neu, and D. McDowell, "Effect of Pre-Exposure on Crack Initiation Life of a Directionally Solidified Ni-Base Superalloy," International Journal of Fatigue 31 (2), 393–401 (2009).
36. G.T. Cashman, "Review Of Competing Modes Fatigue Behavior," International Journal Of Fatigue 32 (3), 492–496 (2010).
37. K.S. Ravi Chandran, P. Chang, and G.T. Cashman, "Competing Failure Modes And Complex S–N Curves In Fatigue Of Structural Materials," International Journal Of Fatigue 32 (3), 482–491 (2010).
38. Y. Kadioglu and H. Sehitoglu, "Thermomechanical and Isothermal Fatigue Behavior of Bare and Coated Superalloys," Journal of Engineering Materials and Technology 118 (1), 94–102 (1996).
39. A. Karabela, L.G. Zhao, B. Lin, J. Tong, and M.C. Hardy, "Oxygen Diffusion And Crack Growth For A Nickel-Based Superalloy Under Fatigue-Oxidation Conditions," Materials Science and Engineering: A 567, 46–57 (2013).
40. A. Karabela, L.G. Zhao, J. Tong, N.J. Simms, J.R. Nicholls, and M.C. Hardy, "Effects of Cyclic Stress and Temperature on Oxidation Damage of a Nickel-Based Superalloy," Materials Science and Engineering: A 528 (19–20), 6194–6202 (2011).
41. H.S. Kitaguchi, H.Y. Li, H.E. Evans, R.G. Ding, I.P. Jones, G. Baxter, and P. Bowen, "Oxidation Ahead of a Crack Tip in an Advanced Ni-Based Superalloy," Acta Materialia 61 (6), 1968–1981 (2013).
42. C.F. Miller, G.W. Simmons, and R.P. Wei, "Evidence For Internal Oxidation During Oxygen Enhanced Crack Growth In P/M Ni-Based Superalloys," Scripta Materialia 48 (1), 103–108 (2003).
43. F. Pettit, "Hot Corrosion of Metals and Alloys," Oxidation of Metals 76 (1–2), 1–21 (2011).
44. D.J. Young, *High Temperature Oxidation and Corrosion af Metals*. (Elsevier, 2008).
45. N. Birks, G.H. Meier and F.S. Pettit, *Introduction to the High Temperature Oxidation of Metals* (Cambridge University Press, 2006).
46. H.L. Cockings, K.M. Perkins, and M. Dowd, "Influence of Environmental Factors on the Corrosion-Fatigue Response of a Nickel-Based Superalloy," Materials Science and Technology 33 (9), 1048–1055 (2017).
47. J. Nesbitt and S. Draper, "Pit Morphology and Depth After Low-Temperature Hot Corrosion of a Disc Alloy," Materials at High Temperatures 33 (4–5), 501–516 (2016).
48. N. Birbilis and R.G. Buchheit, "Measurement and Discussion of Low-Temperature Hot Corrosion Damage Accumulation upon Nickel-Based Superalloy Rene 104," Metallurgical and Materials Transactions A 39 (13), 3224–3232 (2008).
49. D.J. Child, J. Meldrum, and P. Onwuarolu, "Corrosion-Fatigue Testing Of Ni-Based Superalloy RR1000," Materials Science and Technology 33 (9), 1040–1047 (2017).
50. J.K. Sahu, B. Ravi Kumar, S.K. Das, N. Paulose, and S.L. Mannan, "Isothermal High Temperature Low Cycle Fatigue Behavior of Nimonic-263: Influence of Type I and Type II Hot Corrosion," Materials Science and Engineering: A 622, 131–138 (2015).
51. S.L. Li, X.G. Yang, H.Y. Qi, L.Q. Ma, J.S. Yang, and D.Q. Shi, "Experimental Investigation and Life Prediction of Hot Corrosion Pre-Exposure on Low-Cycle fatigue of a Directionally Solidified Nickel-base Superalloy," Fatigue & Fracture of Engineering Materials & Structures 38 (10), 1155–1166 (2015).
52. X. Yang, S. Li, and H. Qi, "Effect of High-Temperature Hot Corrosion on the Low Cycle Fatigue Behavior of a Directionally Solidified Nickel-Base Superalloy," International Journal of Fatigue 70, 106–113 (2015).

53. H. Rosier, K. Perkins, A. Girling, J. Leggett, and G. Gibson, "Factors Affecting the Corrosion Fatigue Life in Nickel Based Superalloys for Disc Applications," MATEC Web of Conferences, 14, p. 03001. EDP Sciences, 2014.
54. G.S. Mahobia, N. Paulose, and V. Singh, "Hot Corrosion Behavior of Superalloy IN718 at 550 and 650 °C," Journal of Materials Engineering and Performance 22 (8) 2418–2435 (2013).
55. G.S. Mahobia, N. Paulose, S.L. Mannan, R.G. Sudhakar, K. Chattopadhyay, N.C. Santhi Srinivas, and V. Singh, "Effect of Hot Corrosion on Low Cycle Fatigue Behavior of Superalloy IN718," International Journal of Fatigue 59, 272–281 (2014).
56. J.K. Sahu, R.K. Gupta, J. Swaminathan, N. Paulose, and S.L. Mannan, "Influence of Hot Corrosion on Low Cycle Fatigue Behavior of Nickel Base Superalloy SU 263," International Journal of Fatigue 51, 68–73 (2013).
57. G. Jianting, D. Ranucci, E. Picco, and P.M. Strocchi, "Effect of Environment on the Low Cycle Fatigue Behaviour of Cast Nickel-Base Superalloy IN738LC," International Journal of Fatigue 6 (2), 95–99 (1984).
58. G. Jianting, D. Ranucci, and E. Picco, "Low Cycle Fatigue Behaviour of Cast Nickel-Base Superalloy IN-738LC in Air and in Hot Corrosive Environments," Materials Science and Engineering 58 (1), 127–133 (1983).
59. J. Telesman, T.P. Gabb, Y. Yamada, and S.L. Draper, "Fatigue Resistance of a Hot Corrosion Exposed Disk Superalloy at Varied Test Temperatures," Materials at High Temperatures 33 (4–5), 517–527 (2016).
60. X. Yang, S. Li, and H. Qi, "Effect of MCrAlY Coating on the Low-Cycle Fatigue Behavior of a Directionally Solidified Nickel-Base Superalloy at Different Temperatures," International Journal of Fatigue 75, 126–134 (2015).
61. T.N. Rhys-Jones and T.P. Cunningham, "The Influence of Surface Coatings on the Fatigue Behaviour of Aero Engine Materials," Surface and Coatings Technology 42 (1), 13–19 (1990).
62. K. Schneider, H. Von Arnim, and H.W. Grünling, "Influence of Coatings and Hot Corrosion on the Fatigue Behaviour Of Nickel-Based Superalloys," Thin Solid Films 84 (1), 29–36 (1981).
63. H.-Y. Qi, J.-S. Yang, X.-G. Yang, S.-L. Li, and L.-Q. Ma, "Fatigue Behavior of Uncoated and MCrAlY-Coated DS Nickel-Based Superalloys Pre-Exposed in Hot Corrosion Condition," Rare Metals 37 (11), 936–941 (2017).
64. K. Rahmani and S. Nategh, "Influence of Aluminide Diffusion Coating on Low Cycle Fatigue Properties of René 80," Materials Science and Engineering: A 486 (1–2), 686–695 (2008).
65. G.A. Whitlow, R.L. Johnson, W.H. Pridemore, and J.M. Allen, "Intermediate Temperature, Low-Cycle Fatigue Behavior of Coated and Uncoated Nickel Base Superalloys in Air and Corrosive Sulfate Environments," Journal of Engineering Materials and Technology 106 (1), 43–49 (1984).
66. Y. Itoh, M. Saitoh, and Y. Ishiwata, "Influence of High-Temperature Protective Coatings on the Mechanical Properties of Nickel-Based Superalloys," Journal of Materials Science 34 (16), 3957–3966 (1999).
67. K. Obrtlík, S. Pospíšilová, M. Juliš, T. Podrábský, and J. Polák, "Fatigue Behavior of Coated and Uncoated Cast Inconel 713LC at 800 °C," International Journal of Fatigue 41, 101–106 (2012).
68. S. Li, X. Yang, H. Qi, G. Xu, and D. Shi, "Influence of MCrAlY Coating on Low-Cycle Fatigue Behavior of a Directionally Solidified Nickel-Based Superalloy in Hot Corrosive Environment," Materials Science and Engineering: A 678, 57–64 (2016).
69. C. Chen, X. Yan, X. Zhang, Y. Zhang, M. Gui, and M. Tao, "Effect of Aluminized Coating on Combined Low and High Cycle Fatigue (CCF) Life of Turbine Blade at Elevated Temperature," Journal of Engineering for Gas Turbines and Power 141 (3), 031018-031018-7 (2018).

70. Y. Itoh, M. Saitoh, K. Takaki, and K. Fujiyama, “Effect of High-Temperature Protective Coatings on Fatigue Lives of Nickel-Based Superalloys,” Fatigue & Fracture of Engineering Materials & Structures 24 (12), 843–854 (2001).
71. T.N. Rhys-Jones, “Protective Oxide Scales on Superalloys and Coatings Used in Gas Turbine Blade and Vane Applications,” Materials Science and Technology 4 (5), 421–430 (1988).
72. G.M. Ecer and G.H. Meier, “Oxidation of High-Chromium Ni-Cr Alloys,” Oxidation of Metals 13 (2), 119–158 (1979).
73. T.P. Gabb, J. Gayda, J. Telesman, and P.T. Kantzos, “Thermal and Mechanical Property Characterization of the Advanced Disk Alloy LSHR,” NASA/TM—2005-213645, Washington, D.C., June 2005.
74. T.P. Gabb, J. Telesman, P.T. Kantzos, and K. O'Connor, “Characterization of the Temperature Capabilities of Advanced Disk Alloy ME3,” NASA/TM—2002-211796, Washington, D.C., August 2002.
75. C.W. Bale, E. Bélisle, P. Chartrand, S.A. Decterov, G. Eriksson, A.E. Gheribi, K. Hack, I.-H. Jung, Y.-B. Kang, and J. Melançon, “FactSage Thermochemical Software and Databases, 2010–2016,” Calphad 54, 35–53 (2016).
76. Donald M. Mattox, “Handbook of Physical Vapor Deposition (PVD) Processing: Film Formation, Adhesion, Surface Preparation and Contamination Control,” Noyes Publications; ISBN: 0-8155-1422-0, pp. 471–474 (1998).
77. J.-O. Andersson, T. Helander, L. Höglund, P. Shi, and B. Sundman, “Thermo-Calc & DICTRA, Computational Tools for Materials Science, TCBin Database,” Calphad 26 (2), 273–312 (2002).
78. J.A. Nesbitt and T.P. Gabb, “LCF Life of NiCr-Y Coated Disk Alloys after Shot Peening, Oxidation and Hot Corrosion,” to be published as NASA TM, NASA Glenn Research Center, Cleveland, OH, (2019).
79. M.I. Wood, “Mechanical Interactions Between Coatings and Superalloys Under Conditions of Fatigue,” Surface and Coatings Technology 39, 29–42 (1989).
80. J.A. Nesbitt and T.P. Gabb, “Effect of Pre-Coat Surface Treatment on the LCF Life of NiCr-Y Coatings for Oxidation and Hot Corrosion Protection of Disk Alloys,” Unpublished research, NASA Glenn Research Center, Cleveland, OH, (2017).